



## ISTITUTO NAZIONALE DI RICERCA METROLOGICA Repository Istituzionale

NextGenPB: An analytically-enabled super resolution tool for solving the Poisson-Boltzmann equation featuring local (de)refinement

*Original*

NextGenPB: An analytically-enabled super resolution tool for solving the Poisson-Boltzmann equation featuring local (de)refinement / Di Florio, Vincenzo; Ansalone, Patrizio; Siryk, Sergii V.; Decherchi, Sergio; De Falco, Carlo; Rocchia, Walter. - In: COMPUTER PHYSICS COMMUNICATIONS. - ISSN 0010-4655. - 317:(2025). [10.1016/j.cpc.2025.109816]

*Availability:*

This version is available at: 11696/88640 since: 2026-02-28T15:14:32Z

*Publisher:*

Elsevier

*Published*

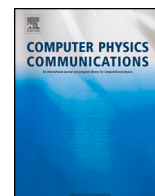
DOI:10.1016/j.cpc.2025.109816

*Terms of use:*

This article is made available under terms and conditions as specified in the corresponding bibliographic description in the repository



*Publisher copyright*

(Article begins on next page)



## Computational Physics

## NextGenPB: An analytically-enabled super resolution tool for solving the Poisson-Boltzmann equation featuring local (de)refinement

Vincenzo Di Florio<sup>a,b,c</sup>, Patrizio Ansalone<sup>d</sup>, Sergii V. Siryk<sup>a, </sup>, Sergio Decherchi<sup>e</sup>, Carlo de Falco<sup>c</sup>, Walter Rocchia<sup>a, ,\*</sup>

<sup>a</sup> CONCEPT Lab, Fondazione Istituto Italiano di Tecnologia, Via E. Melen 83, Genova, 16152, Italy

<sup>b</sup> Department of Mathematical Sciences, Politecnico di Torino, Corso Duca degli Abruzzi, 24, Torino, 10129, Italy

<sup>c</sup> MOX Laboratory, Department of Mathematics, Politecnico di Milano, Piazza Leonardo Da Vinci, 32, Milano, 20133, Italy

<sup>d</sup> Advanced Materials Metrology and Life Sciences, Istituto Nazionale di Ricerca Metrologica, Strada delle Cacce, 91, Torino, 10135, Italy

<sup>e</sup> Data Science and Computation, Fondazione Istituto Italiano di Tecnologia, Via Morego 30, Genova, 16163, Italy

## ARTICLE INFO

The review of this paper was arranged by Prof. W. Jong

MSC:  
65N30  
35Q92

Keywords:  
Poisson-Boltzmann  
Continuum electrostatics  
Finite-element method  
Analytical PDE solutions  
PBE solver

## ABSTRACT

The Poisson-Boltzmann equation (PBE) is a relevant partial differential equation commonly used in biophysical applications to estimate the electrostatic energy of biomolecular systems immersed in electrolytic solutions. A conventional mean to improve the accuracy of its solution, when grid-based numerical techniques are used, consists in increasing the resolution, locally or globally. This, however, usually entails higher complexity, memory demand and computational cost. Here, we introduce NextGenPB, a linear PBE, adaptive-grid, FEM-based solution tool that leverages analytical calculations to maximize the accuracy-to-computational-cost ratio. Indeed, in NextGenPB (aka NGPB), analytical corrections at the surface of the solute enhance the solution's accuracy without requiring grid adaptation. This leads to more precise estimates of the electrostatic potential, fields, and energy at no perceptible additional cost. Also, we apply computationally efficient yet accurate boundary conditions by taking advantage of local grid de-refinement. To assess the accuracy of our methods directly, we expand the traditionally available analytical case set to many non-overlapping dielectric spheres. Then, we use an existing benchmark set of real biomolecular systems to evaluate the energy convergence concerning grid resolution. Thanks to these advances, we have improved state-of-the-art results and shown that the approach is accurate and largely scalable for modern high-performance computing architectures. Lastly, we suggest that the presented core ideas could be instrumental in improving the solution of other partial differential equations with discontinuous coefficients.

## 1. Introduction

The Poisson-Boltzmann equation (PBE) is a cornerstone of electrostatic modeling in soft matter physics, biophysics, and colloidal science [1,2]. It plays a crucial role in understanding how charged particles interact in various environments, including biological systems, colloidal suspensions, and electrolytic solutions. At its core, the PBE provides a mathematical framework to describe the mean field electrostatic potential generated by a distribution of fixed charges in a dielectric medium immersed in another one. The latter is usually a more polarizable dielectric medium representing the solvent and containing mobile ions, described as potential-dependent distributions [3].

In biological systems, the PBE is a crucial instrument for modeling interactions at the molecular level, such as protein-protein binding, nucleic acid stability, and enzyme activity. It helps predict how biomolecules behave in different ionic environments, a critical factor in drug design, molecular recognition, and understanding the stability of macromolecular structures. Beyond biology, the PBE is equally essential in materials science, where it is used to predict the behavior of colloidal particles, understand self-assembly processes, and design new materials with specific electrostatic properties.

The PBE is inherently nonlinear, making it challenging to solve analytically or even numerically. For many practical applications, however, the linearized version of the PBE (LPBE) is used, especially when the

\* Corresponding author.

E-mail address: [walter.rocchia@iit.it](mailto:walter.rocchia@iit.it) (W. Rocchia).

system involves low surface potentials. However, even the LPBE requires sophisticated mathematical techniques and numerical methods for its accurate resolution, particularly in complex geometries or large-scale systems. Indeed, the model used to describe the molecular surface (MS) has great impact on the potential resulting from the solution of the equation [4,5], and it has been shown that subtle, but still biologically relevant, effects descend from the intricate geometries of the MS [6].

Advances in computational methods have made it possible to tackle the PBE with greater precision [7], allowing for more detailed and accurate modeling of electrostatic interactions in various systems. These developments have led to new insights into phenomena like ion binding, charge screening, and the stabilization of charged interfaces, further solidifying the PBE as an essential tool in the study of electrostatics.

Present challenges for this approach are its ability to describe large systems (as those observed by Cryo-EM experimental techniques), its accuracy in matching experimental energies and local electric fields [8,9], its computational cost, an essential requirement for its highly repetitive execution required by pKa states description [10] or Constant-pH Molecular Dynamics simulations [11]. These considerations fuel the quest for more efficient resolution techniques, which will strengthen and expand their applicability and offer more profound insights into the behavior of charged systems at both the macroscopic and microscopic levels.

In this work, we present several advances in the model and in the resolution of the LPBE, where the contribution of analytical calculations is instrumental in improving the solution's accuracy without increasing the computational cost. Namely, we use the analytical information on the MS, as provided by the NanoShaper software [5,12] to enable a local Taylor expansion for the electrostatic potential at the MS, which in turn is used to improve the discretization of the equation. By suitable use of Green's identities, we also derive an expression for the interaction between the solvent counterions and the charges of the solute, which avoids integrating over the entire solvent volume. Finally, we propose to use a variable-resolution grid to apply accurate boundary conditions (BCs) at a limited computational cost. To validate the improved accuracy of the method, we compare with analytical expressions for a system of many charged, non-overlapping, dielectric spheres immersed in a Debye-Hückel solvent. Next, we apply the method to systems of biological interest, namely proteins and nucleic acids. The proposed advances are implemented in NextGenPB, a Finite Element Method Poisson-Boltzmann (PB) solver, which is made available at <https://github.com/concept-lab/NextGenPB> or <https://concept.iit.it/downloads>. In the following sections, we discuss the enhanced solution method, present experimental results and provide a final discussion and conclusions.

## 2. Physical models and mathematical foundations

### 2.1. Poisson-Boltzmann equation

Consider a bounded domain  $D = \Omega_m \cup \Omega_s \cup \Gamma$ , where  $\Omega_m$  represents the region of space occupied by the solute (usually a molecule),  $\Omega_s$  is the solvent region, and  $\Gamma$  is the closed surface separating them. In the context of biomolecular electrostatics calculations, a molecule is represented as a union of possibly overlapping linear dielectric balls, the atoms, immersed in a high-dielectric solvent. The relative dielectric constant of the solute,  $\epsilon_{r,m}$  usually ranges between 2 and 4, reflecting the electronic polarization of the molecule. The solute contains all the explicitly assigned partial charges centered on atoms. In contrast,  $\epsilon_{r,s}$ , i.e., the solvent's relative dielectric constant, is higher, nearly 80, accounting for the presence of mobile ions that respond to the local electrostatic potential. From the physical point of view, both atomic charges and mobile ions constitute the free charge. Still, there is a significant modelistic distinction between them since the former is assigned as an input to the equation. At the same time, the ionic density results from the calculation since the model prescribes a relationship between the ionic response and the local electric field.

In this context, the polarization response is described by a piece-wise constant dielectric function:

$$\epsilon(\mathbf{r}) = \begin{cases} \epsilon_m = \epsilon_0 \epsilon_{r,m} & \text{if } \mathbf{r} \in \Omega_m \\ \epsilon_s = \epsilon_0 \epsilon_{r,s} & \text{if } \mathbf{r} \in \Omega_s \end{cases}, \quad (1)$$

where  $\epsilon_0$  is the vacuum permittivity, and  $\epsilon_m$  and  $\epsilon_s$  are the permittivities of molecule and solvent, respectively. Gauss's law can describe the electrostatics of this system for the electric displacement in differential form:

$$\nabla \cdot (\epsilon(\mathbf{r}) \nabla \phi) = -\rho^{free} = -\rho^f - \rho^s \quad \mathbf{r} \in D, \quad (2)$$

where  $\rho^f$  is the fixed charge density present only inside the molecule, and  $\rho^s$  is the ionic charge present only in the solvent. The fixed charge density, composed of point charges, is defined as:

$$\rho^f(\mathbf{r}) = \sum_{i=1}^N q_i \delta(\mathbf{r} - \mathbf{r}_i) \quad (3)$$

where  $\mathbf{r}_i$  is the position of the  $i$ -charge. The concentrations of the different ionic species inside the solvent can be described by assuming that the charge carriers are immaterial, that only feel the local electrostatic potential and the thermal bath and that they obey the overall electroneutrality condition:  $\sum_{j=1}^J z_j e \rho_j^b = 0$ , where  $J$  is the number of ionic species,  $e$  is the charge of a proton, and  $z_j$  and  $\rho_j^b$  denote the valence and bulk concentration of ions of species  $j$ , respectively. Under these assumptions, one can impose that, at thermal equilibrium, the local concentration of each species is related to that of the same species in the bulk by a Boltzmann weight. This leads to the following expression for the charge density in the solvent:

$$\rho^s(\mathbf{r}) = \sum_{j=1}^J e z_j \rho_j^b \exp \left[ -\frac{e z_j \phi(\mathbf{r})}{K_b T} \right] \chi_{\Omega_s}(\mathbf{r}) \quad (4)$$

( $K_b$  and  $T$  are Boltzmann's constant and absolute temperature, respectively).

Since the ions are only located in the solvent, the characteristic function  $\chi_{\Omega_s}$  equals 1 when  $\mathbf{r} \in \Omega_s$  and 0 elsewhere. This yields the Poisson-Boltzmann equation:

$$\nabla \cdot (\epsilon(\mathbf{r}) \nabla \phi) = -\sum_{i=1}^N q_i \delta(\mathbf{r} - \mathbf{r}_i) - \sum_{j=1}^J \left[ e z_j \rho_j^b \exp \left\{ -\frac{e z_j \phi(\mathbf{r})}{K_b T} \right\} \right] \chi_{\Omega_s}(\mathbf{r}) \quad (5)$$

In case the Stern layer model is used,  $\chi_{\Omega_s} = 0$  also inside it. For low-charged systems, the resulting potential in solution may satisfy the following relationship:  $|\frac{e z_j \phi(\mathbf{r})}{K_b T}| \ll 1$ . Under this and electroneutrality assumptions, the local concentration of ions in the solvent can be approximated as a linear function of the potential:

$$\rho^s(\mathbf{r}) \approx -\epsilon_s k_D^2 \chi_{\Omega_s}(\mathbf{r}) \phi(\mathbf{r}) = -c(\mathbf{r}) \phi(\mathbf{r}), \quad (6)$$

where  $k_D = \sqrt{\frac{e^2}{\epsilon_s K_b T} \sum_{j=1}^J z_j^2 \rho_j^b}$  is the Debye factor for the solution, reciprocal of the so-called Debye screening length. This approximation leads to the Debye-Hückel (D-H), or linear Poisson-Boltzmann equation (LPBE):

$$\nabla \cdot (\epsilon(\mathbf{r}) \nabla \phi) = -\sum_{i=1}^N q_i \delta(\mathbf{r} - \mathbf{r}_i) + c(\mathbf{r}) \phi(\mathbf{r}) \quad \mathbf{r} \in D. \quad (7)$$

Equation (7) is a linear, elliptic partial differential equation. It is more manageable numerically and analytically than its nonlinear counterpart, making it the most commonly used equation for studying the electrostatics of biomolecular systems.

## 2.2. Electrostatic energy

The derivation of the energy of a system described by linear Poisson-Boltzmann model with  $N$  fixed point charges in the solute can be found, for instance, in [13] and it takes the form:

$$E = \frac{1}{2} \int_{\Omega_m} \rho^f(\vec{r}) \phi(\vec{r}) dV = \frac{1}{2} \sum_{i=1}^N q_i \phi(\mathbf{r}_i), \quad (8)$$

where  $\phi$  is the total potential, excluding the so-called self-potential, which is the one generated by  $q_i$  at  $\mathbf{r}_i$ .  $E$  can be considered the electrostatic component of a solvated system's free energy, where the solvent's degrees of freedom have been averaged out. A convenient way to represent the electrostatic energy (8) is given in work [14], where the total potential is partitioned in three contributions: the Coulombic term  $\phi_{coul}$ , which can be calculated analytically, the  $\phi_{pol}$  term, due to the polarization charges arising at the MS where the dielectric constant varies, and  $\phi_{ion}$ , the potential generated by the counterions in the solvent. Both  $\phi_{coul}$  and  $\phi_{ion}$  account for the screening due to the continuum medium in which their sources are located.

$$E = \frac{1}{2} \sum_{i=1}^N q_i (\phi_{coul}(\mathbf{r}_i) + \phi_{pol}(\mathbf{r}_i) + \phi_{ion}(\mathbf{r}_i)). \quad (9)$$

This partitioning of the potential and, consequently, of the energy allows for the analytical estimation of the Coulombic term, avoiding the self-energy, and for the calculation of the polarization term. As per the ionic term, its source is the local ionic imbalance, which extends over the entire solvent until where the potential vanishes. Since volume integration of this latter term, which turns out to be overall smaller than the previous ones, is prohibitive, it is usually avoided. Alternatively, the ionic energy contribution can be calculated by taking the difference of the so-called *grid energy* in two successive runs at different ionic strengths, namely 0 and the actual one. Grid energy is half the sum of the fixed charges mapped onto the grid points times the numeric potential evaluated at the corresponding points.

## 2.3. Electrostatic potential partitioning

In this section, we use two expressions for the electrostatic potential partitioning based on Green's identities, one when the potential is evaluated inside the solute and the other when it is evaluated in the solvent. They are derived in Appendix A and Appendix C. These formulations are convenient for practical energy calculation and for assessing the quality of existing boundary conditions.

Let's consider the potential evaluated at a point  $\mathbf{r}$  belonging to a volume region  $\Omega_m$  enclosed in a surface  $\Gamma$ . This region, that in the PB case represents the solute, is surrounded by the electrolytic solution, and contains the free charge distribution  $\rho^f$ . As shown in Appendix A, this potential can be expressed as follows  $\forall \mathbf{r} \in \Omega_m$ :

$$\begin{aligned} \phi(\mathbf{r}) = & \int_{\Omega_m} \frac{\rho^f}{4\pi\epsilon_m \|\vec{r} - \mathbf{r}\|} dV - \int_{\Gamma} \frac{\mathbf{D}(\vec{r}) \cdot \mathbf{n}(\vec{r})}{4\pi\epsilon_m \|\vec{r} - \mathbf{r}\|} dS \\ & + \int_{\Gamma} \phi(\vec{r}) \frac{(\vec{r} - \mathbf{r}) \cdot \mathbf{n}(\vec{r})}{4\pi \|\vec{r} - \mathbf{r}\|^3} dS. \end{aligned} \quad (10)$$

The first term in the right-hand side (RHS) is  $\phi_{coul}$ , that is the Coulombic part of the potential.

In agreement with the continuum electrostatic model, the surface polarization charge is distributed on  $\Gamma$ , and it is equal to:

$$\sigma_{pol}(\mathbf{r}) = -(\mathbf{P}_2(\mathbf{r}) - \mathbf{P}_1(\mathbf{r})) \cdot \mathbf{n}_{21}(\mathbf{r}) \quad \mathbf{r} \in \Gamma, \quad (11)$$

where  $\mathbf{n}_{21}$  is the unit normal pointing from the molecule to the solvent, and  $\mathbf{P}_1(\mathbf{r})$  and  $\mathbf{P}_2(\mathbf{r})$  are the polarization vectors in the molecule and in the solvent respectively, evaluated at  $\mathbf{r} \in \Gamma$ . Therefore, the surface polarization charge in this system is:

$$\sigma_{pol}(\mathbf{r}) = \epsilon_0 \left( \frac{1}{\epsilon_s} - \frac{1}{\epsilon_m} \right) \mathbf{D}(\mathbf{r}) \cdot \mathbf{n}(\mathbf{r}) \quad \mathbf{r} \in \Gamma, \quad (12)$$

and the corresponding potential is:

$$\phi_{pol}(\mathbf{r}) = \int_{\Gamma} \frac{\sigma_{pol}(\vec{r})}{4\pi\epsilon_0 \|\vec{r} - \mathbf{r}\|} dS = \left( \frac{1}{\epsilon_s} - \frac{1}{\epsilon_m} \right) \int_{\Gamma} \frac{\mathbf{D}(\vec{r}) \cdot \mathbf{n}(\vec{r})}{4\pi \|\vec{r} - \mathbf{r}\|} dS. \quad (13)$$

Considering this term, we can rewrite the potential in Eq. (10) to make the polarization term more explicit:

$$\begin{aligned} \phi(\mathbf{r}) = & \phi_{coul}(\mathbf{r}) + \left( \frac{1}{\epsilon_s} - \frac{1}{\epsilon_m} \right) \int_{\Gamma} \frac{\mathbf{D}(\vec{r}) \cdot \mathbf{n}(\vec{r})}{4\pi \|\vec{r} - \mathbf{r}\|} dS \\ & + \int_{\Gamma} \phi(\vec{r}) \frac{(\vec{r} - \mathbf{r}) \cdot \mathbf{n}(\vec{r})}{4\pi \|\vec{r} - \mathbf{r}\|^3} dS - \frac{1}{\epsilon_s} \int_{\Gamma} \frac{\mathbf{D}(\vec{r}) \cdot \mathbf{n}(\vec{r})}{4\pi \|\vec{r} - \mathbf{r}\|} dS \end{aligned} \quad \forall \mathbf{r} \in \Omega_m. \quad (14)$$

When comparing Eq. (14) with (9), one can immediately identify the sum of the last two terms as the potential due to the ionic charge density in the solution. This expression, explicitly derived in Appendix B, converts a volumetric term extending over a possibly huge domain into a much more localized surface term. This equivalence is particularly convenient for calculating the ionic direct energy term in just one solving process, in contrast, for instance, to what is described in Sect. 2.2, as it will be shown in Sect. 3.3.2.

One could repeat a similar analysis employing Green's identities when considering the potential in the solvent region. Following the derivation performed in Appendix C, this leads to the following formulation for the electrostatic potential outside the molecule  $\forall \mathbf{r} \in \Omega_s$ :

$$\begin{aligned} \phi(\mathbf{r}) = & \int_{\text{Stern layer}} \phi(\vec{r}) \frac{k_D^2 e^{-k_D \|\vec{r} - \mathbf{r}\|}}{4\pi \|\vec{r} - \mathbf{r}\|} dV + \int_{\Gamma} \frac{e^{-k_D \|\vec{r} - \mathbf{r}\|} \mathbf{D}(\vec{r}) \cdot \mathbf{n}(\vec{r})}{4\pi\epsilon_s \|\vec{r} - \mathbf{r}\|} dS + \\ & - \int_{\Gamma} \phi(\vec{r}) \frac{e^{-k_D \|\vec{r} - \mathbf{r}\|} (1 + k_D \|\vec{r} - \mathbf{r}\|) (\vec{r} - \mathbf{r}) \cdot \mathbf{n}(\vec{r})}{4\pi \|\vec{r} - \mathbf{r}\|^3} dS. \end{aligned} \quad (15)$$

As customary in continuum electrostatics, this can be interpreted as the sum of the potential generated by a surface charge distributed on the MS, of that generated by a layer of ideal dipoles located also on the MS, plus a contribution spread over the Stern layer. The electrolytic solution screens all of these sources of potential. This expression will be used in Sect. 2.4 to assess the quality of existing boundary conditions.

## 2.4. Boundary conditions

Choosing convenient boundary conditions is essential in setting up the PBE solution. Physical considerations tell us that the electrostatic potential and field are expected to approach zero at a sufficient distance from the region where the fixed charges are located. Consequently, suitable boundary conditions could be the homogeneous Dirichlet ones, where the potential is set to zero at the boundary of the solution domain. However, this can be acceptable only if the *perfil*, that is the ratio between the size of the solute and that of the computational domain, is relatively small. To allow a larger *perfil*, analytical approximations for the potential at an intermediate distance from the solute are often used. For example, the so-called Coulombic or, better, Debye-Hückel boundary conditions. If one considers a system with  $N$  fixed charges and a solvent containing a dissociated monovalent salt, the D-H solution takes the form:

$$\phi(\mathbf{r}) = \sum_{i=1}^N \frac{q_i e^{-k_D \|\vec{r} - \mathbf{r}\|}}{4\pi\epsilon_s \|\vec{r} - \mathbf{r}\|}. \quad (16)$$

There are two main differences between the potential generated by this model, which has been called the "fully penetrating solvent" model [15],

and a more realistic one, where the charges are not directly exposed to the solvent but are instead embedded into a low dielectric solute. One is that the approximated potential misses the dipolar contribution originated in the low-polarization medium. The other is that counterions in the approximated model occupy the region that in reality is occupied by the low dielectric medium. This second term is more impactful than the first, which decays as a screened dipolar potential does. Suppose we consider the simplest among the few known analytical solutions for the LPBE, namely the spherical case. In that case, we can easily derive the exact potential outside a sphere of the radius  $R$  with a single charge  $q$  located in its center:

$$\phi(r) = \frac{q}{4\pi\epsilon_s r(1+k_D R)} e^{-k_D(r-R)} = \phi_{coul}(r) \frac{e^{k_D R}}{(1+k_D R)} \quad (17)$$

It can be easily seen that the difference between the actual potential and its D-H approximation tends to zero of the same order as the actual potential does, so the D-H approximation cannot be considered an actual asymptotic solution.

Let's now consider the most general case of Eq. (15). We observe that the first two terms are prevalent at larger distances than the second one, since the potential generated by a dipole layer decays faster than that of a surface charge. One can thus conclude, at least qualitatively, that a more accurate asymptotic solution should be written as the sum of Debye-Hückel-like terms centered on points lying on the MS or in the Stern layer. This consideration, however, does not provide details on the parameters of these terms, since their knowledge requires that of the electric displacement at the MS, which become available only after the PBE is solved. Along the same qualitative lines, one could expect that the discrepancy between the actual potential and that obtained by the penetrating solvent approximation should increase with the volume of the solute, which excludes more counterions, and with its absolute net charge, which reduces the possibility of cancellations in the ionic reaction.

### 3. The numerical model

In devising a convenient discretization strategy for the model described above, we have been guided by two main objectives: on the one hand, we want to achieve the best possible accuracy for the electrostatic potential and energy calculation near the molecular surface where the discontinuity occurs; on the other hand, the extreme size of the problems typically being considered demands for a discretization scheme generating matrices with simple structure and small stencil. To attain the former goal, we adopt special quadrature formulas based on the physically motivated averaging of the electrical permittivity introduced in Sect. 3.2. To achieve the latter goal, we limit the complexity of the discretization stencils by working with low order Finite Element basis functions on a Cartesian grid, and applying a reduced integration [16] approach. Our discretization method can be represented as a mixed formulation of the elliptic PDE at hand, *i.e.*, we start by reformulating the second order differential problem as a system of two first order problems and then we choose suitable function spaces to represent both the *primal variable* (the electrostatic potential  $\phi$ ) and the *dual variable* (the electric displacement vector  $\mathbf{D}$ ). In particular, we use the primal-mixed formulation [17,18], whereby global continuity of  $\phi$  is enforced, while a partially discontinuous representation of  $\mathbf{D}$  is tolerated. We then eliminate the degrees of freedom related to the dual variable, a procedure commonly referred to as *static condensation* [19]. Hierarchical (de)refinement also allows for a significant reduction of the problem unknowns and is a crucial feature of our implementation. The approach used to accommodate for non-conforming meshes with so-called *hanging nodes* is described in some detail in previous work [20,21] therefore, in Sect. 3.1 we assume that, for sake of brevity and readability, our discretization domain consists of a full tensor-product Cartesian grid.

#### 3.1. Primal-mixed finite elements discretization of the LPBE

As already mentioned above, we start the derivation by formulating LPBE (7), over a domain  $D \subset \mathbb{R}^3$  as a system of two first order equations:

$$\begin{cases} \frac{1}{\epsilon} \mathbf{D} + \nabla \phi = 0 \\ \nabla \cdot \mathbf{D} + c \phi = \rho^f. \end{cases} \quad (18)$$

We assume for the time being that homogeneous Dirichlet-type Boundary conditions are to be enforced on the whole boundary  $\partial D$  of  $D$ , albeit a more in-depth discussion of BCs has been dealt with in Sect. 2.4.

In order to numerically solve (18) via a Galerkin/Finite Element approximation we must, first of all, state the problem in its weak form. To this end, we multiply both equations in (18) by suitable *test functions* and perform integration by parts to obtain:

$$\text{find } (\mathbf{D}, \phi) \in U \times W \text{ such that } \forall (\boldsymbol{\sigma}, v) \in U \times W:$$

$$\begin{aligned} \int_D \frac{1}{\epsilon} \mathbf{D} \cdot \boldsymbol{\sigma} \, dV + \int_D \nabla \phi \cdot \boldsymbol{\sigma} \, dV &= 0, \\ \int_D \mathbf{D} \cdot \nabla v \, dV - \int_D c \phi v \, dV &= - \int_D \rho^f v \, dV, \end{aligned} \quad (19)$$

where  $U \equiv (L^2(D))^3$  and  $W \equiv H_0^1(D)$ . Introducing the bilinear forms  $a(\cdot, \cdot) : U \times U \rightarrow \mathbb{R}$  and  $b(\cdot, \cdot) : U \times W \rightarrow \mathbb{R}$ ,  $\kappa(\cdot, \cdot) : W \times W \rightarrow \mathbb{R}$  and the linear operator  $R : W \rightarrow \mathbb{R}$ ,

$$\begin{aligned} a(\mathbf{u}, \mathbf{z}) &= \int_D \frac{1}{\epsilon} \mathbf{u} \cdot \mathbf{z} \, dV, \\ b(\mathbf{u}, v) &= \int_D \mathbf{u} \cdot \nabla v \, dV, \\ \kappa(w, v) &= \int_D c w v \, dV, \\ R(v) &= \int_D \rho^f v \, dV, \end{aligned} \quad (20)$$

Eq. (19) becomes:

$$\text{find } (\mathbf{D}, \phi) \in U \times W \text{ s.t.}$$

$$\begin{cases} a(\mathbf{D}, \boldsymbol{\sigma}) + b(\boldsymbol{\sigma}, \phi) = 0 \\ b(\mathbf{D}, v) - \kappa(\phi, v) = -R(v) \end{cases} \quad (21)$$

$$\forall (\boldsymbol{\sigma}, v) \in U \times W.$$

The Galerkin/Finite Element method for the numerical approximation of (21) consists of looking for an approximate solution  $(\mathbf{D}_h, \phi_h) \in U_h \times W_h$ , where

$$W_h \subset W, \quad \dim(W_h) = N_v^h < \infty$$

$$U_h \subset U, \quad \dim(U_h) = N_e^h < \infty$$

are two families of *finite dimensional* subspaces depending on the parametrized by the *mesh size*  $h$ , s.t.  $U_h \rightarrow U$  and  $W_h \rightarrow W$  for  $h \rightarrow 0$ . Then, the discretized version of (21) takes the form:

$$\text{find } (\mathbf{D}_h, \phi_h) \in U_h \times W_h \text{ s.t.}$$

$$\begin{cases} a(\mathbf{D}_h, \boldsymbol{\sigma}) + b(\boldsymbol{\sigma}, \phi_h) = 0 \\ b(\mathbf{D}_h, v) - \kappa(\phi_h, v) = -R(v) \end{cases} \quad (22)$$

$$\forall (\boldsymbol{\sigma}, v) \in U_h \times W_h.$$

In order to guarantee the stability of (22), the chosen pair of finite dimensional spaces  $U_h$  and  $W_h$  must satisfy the Ladyzhenskaya-Babuška-Brezzi (LBB) condition [17,22] which is simply attained if  $\nabla W_h \subset U_h$  [18]. To enforce the latter condition we chose as  $W_h$  the set

of piecewise tri-linear continuous functions on the triangulation, while we let  $U_h$  be comprised of lowest-order Nédélec edge elements of the first kind [23,24]. Denoting by  $\{\sigma_j\}$  a basis of  $U_h$  and by  $\{w_k\}$  a basis of  $W_h$ , we can write  $\mathbf{D}_h$  and  $\phi_h$  as an appropriate linear combination of these bases, i.e.

$$\mathbf{D}_h = \sum_{j=1}^{N_e^h} D_j^h \sigma_j, \quad \phi_h = \sum_{k=1}^{N_v^h} \phi_k^h w_k. \quad (23)$$

We note that the dimension  $N_e^h$  of  $U_h$  is the number of edges in the mesh and dimension  $N_v^h$  of  $W_h$  is the number of interior vertices. We shall then request:

$$\begin{cases} \sum_j D_j^h a(\sigma_j, \sigma_i) + \sum_k \phi_k^h b(\sigma_i, w_k) = 0 & \forall i, \\ \sum_j D_j^h b(\sigma_j, w_n) - \sum_k \phi_k^h \kappa(w_k, w_n) = -R(w_n) & \forall n. \end{cases} \quad (24)$$

The matrix form of (24) is

$$\begin{bmatrix} \tilde{A} & B^T \\ B & -C \end{bmatrix} \begin{bmatrix} \mathbf{D}^h \\ \boldsymbol{\phi}^h \end{bmatrix} = \begin{bmatrix} 0 \\ -\mathbf{R} \end{bmatrix}, \quad (25)$$

where  $\tilde{A} = [a(\sigma_i, \sigma_j)] = [a_{i,j}]$ ,  $B^T = [b(\sigma_i, w_k)] = [b_{i,k}]$ ,  $\mathbf{D}^h = [D_1^h, \dots, D_{N_e^h}^h]$ ,  $\boldsymbol{\phi}^h = [\phi_1^h, \dots, \phi_{N_v^h}^h]$ ,  $C = [\kappa(w_k, w_n)] = [c_{k,n}]$  and  $\mathbf{R} = [R(w_1), \dots, R(w_{N_v^h})]$ .

As anticipated in the introduction to Sect. 3, the structure and bandwidth of the matrices in (25) can be highly simplified by approximating the integrals in (19) by means of low order quadratures. In particular, it is easily shown that, by selecting the cell vertices as quadrature nodes,  $\tilde{A}$ , ends up being a diagonal, and therefore easily invertible, matrix. We can take advantage of the simple form of  $\tilde{A}$  to reduce the total number of unknowns in the systems via a Schur-complement approach (often referred to as *static condensation* in the jargon of Finite Elements practitioners [25]). Indeed, solving the first row of (25) for  $\mathbf{D}^h$  we get

$$\mathbf{D}^h = -\tilde{A}^{-1} B^T \boldsymbol{\phi}^h$$

and plugging the latter into the second row

$$[-B(\tilde{A}^{-1} B^T) - C] \boldsymbol{\phi}^h = \mathbf{A} \boldsymbol{\phi}^h = -\mathbf{R}. \quad (26)$$

As for the choice of the quadrature rule, the obvious choice for a rule with nodes at the vertices is that of the trapezoidal rule; it is easily shown that upon making such choice, the matrices in (26) correspond to those that would be obtained by taking the *harmonic average*, that is the average of the inverses, of the permittivity over the edges and applying a standard Finite Element discretization of the problem [26,27]. In the next sections, we will show how a different choice of the quadrature weights (or equivalently a choice of the averaging coefficients for the permittivity on the edges) can significantly improve the performance of the discretization near the molecular surface.

### 3.2. Coefficient discontinuity: equation discretization across the molecular surface $\Gamma$

As described, for the solution of the LPBE, we opt for an orthogonal cubic finite elements method (FEM). In this scheme, we represent our potential in a first-order Lagrangian basis. According to this description, the potential and similar quantities defined on the nodes are tri-linearly interpolated in off-grid positions. It descends from this approach that the interpolated potential changes are always linear along grid edges, and correspondingly, the electric field is constant on them. This reconstruction scheme perfectly fits the continuum electrostatics model when a grid edge is entirely inside the same medium (solute or solvent). However, it conflicts with the physical model when an edge crosses the surface, separating two different media. Indeed, the continuum electrostatics theory prescribes that the potential is continuous across the jump in dielectric constant, likewise the orthogonal component of the dielectric displacement. This causes a step discontinuity on the electric

field's orthogonal components, which a linear interpolation along adjacent nodes cannot recover. Conventional solutions to this problem can be increasing the grid resolution, possibly locally, using irregular grids to localize the nodes at the discontinuity or changing the shape of the elements so that they better fit that of the MS. All of these solutions, however, entail some increase in the degree of complexity of the method. In our quest for increased accuracy at low computational impact, we note that the information that we can get from NanoShaper [5] is richer than simply telling whether a point is inside or outside the volume enclosed by the MS. We have analytical information related to where exactly the edges intersect the MS, together with the corresponding normal. We aim to use this information to improve how the equation is discretized on the MS-crossing edges.

Let's consider two adjacent nodes, 1 and 2 along a given MS-crossing edge and let's call  $\mathcal{O}$  the point where the edge intersects the MS. Let's then consider the two first-order Taylor expansions of the potential centered at the point of intersection along that edge. One expansion holds in medium 1, while the other in medium 2:

$$\phi(\mathbf{r}_1) = \phi(\mathbf{r}_0^-) - E_\nu(\mathbf{r}) \Big|_{\mathbf{r}_0^-} (r_1^\nu - r_0^{\nu,-}) + O(\|\mathbf{r}_1 - \mathbf{r}_0\|^2), \quad (27)$$

$$\phi(\mathbf{r}_2) = \phi(\mathbf{r}_0^+) - E_\nu(\mathbf{r}) \Big|_{\mathbf{r}_0^+} (r_2^\nu - r_0^{\nu,+}) + O(\|\mathbf{r}_2 - \mathbf{r}_0\|^2), \quad (28)$$

where  $\mathbf{r}_0$  is the exact position of the intersection,  $\mathbf{r}_1$  and  $\mathbf{r}_2$  are the positions of the nodes,  $\nu$  is the coordinate direction of the edge and  $E_\nu$  is the  $\nu$ -component of the electric field. The symbols  $\mathbf{r}_0^-$  and  $\mathbf{r}_0^+$  denote the position's limit values as they approach the surface from the two different media and coincide.

The electric field at the intersection point can be written as the sum of the vector components normal and tangential to the MS. The electric field at the MS is not continuous, but it can be conveniently represented as the sum of its tangential component vector, which is continuous, and of the normal component vector of the electric displacement, also continuous, divided by the local dielectric constant:  $\mathbf{E}(\mathbf{r}_0^\pm) = \mathbf{E}_t(\mathbf{r}_0) + \frac{\mathbf{D}_n(\mathbf{r}_0)}{\epsilon(\mathbf{r}_0^\pm)}$ .

By denoting with  $\alpha$  the edge fraction in medium 1, we obtain  $r_1^\nu - r_0^{\nu,-} = -h_\nu \alpha$  and  $r_2^\nu - r_0^{\nu,+} = h_\nu(1 - \alpha)$ , where  $h_\nu$  is the length of the edge in the direction  $\nu$ . The continuity of  $\phi$  ensures  $\phi(\mathbf{r}_0^-) = \phi(\mathbf{r}_0^+) = \phi(\mathbf{r}_0)$ . Moreover,  $\epsilon(\mathbf{r}_0^-) = \epsilon_1$  and  $\epsilon(\mathbf{r}_0^+) = \epsilon_2$ .

If we now subtract term by term Eq. (28) from (27) while keeping only the linear terms and divide both sides by  $h_\nu$ , we obtain the expression for the incremental ratio of the potential with respect to the grid spacing, which in normal conditions of uniform medium, is the finite difference approximation of the electric field:

$$-\frac{\phi(\mathbf{r}_2) - \phi(\mathbf{r}_1)}{h_\nu} = E_{t\nu}(\mathbf{r}_0) + \frac{D_{n\nu}(\mathbf{r}_0)}{\epsilon^{eff}} =: E_\nu^{eff}, \quad (29)$$

where  $\epsilon^{eff}$  takes the form of the weighted harmonic average (WHA) of  $\epsilon_1$  and  $\epsilon_2$ :

$$\epsilon^{eff} = \frac{1}{\frac{\alpha}{\epsilon_1} + \frac{(1-\alpha)}{\epsilon_2}}. \quad (30)$$

While harmonic averages have already been used in FEM at the crossing of a discontinuity [17,18], this derivation provides a robust physical interpretation, going beyond the intuitive representation of a series of two capacitors, and a more accurate expression in terms of a WHA.

Thus,  $\mathbf{E}^{eff}$  is the electric field corresponding to the correct voltage drop between  $\mathbf{r}_1$  and  $\mathbf{r}_2$ , its tangential component equals that of the actual electric field at  $\mathbf{r}_0$ . The corresponding effective electric displacement is  $\mathbf{D}^{eff} := \epsilon^{eff} \mathbf{E}^{eff} = \mathbf{D}_n(\mathbf{r}_0) + \epsilon^{eff} \mathbf{E}_t(\mathbf{r}_0)$ , its normal component equals that of the actual electric displacement at  $\mathbf{r}_0$ . This construction provides a convenient expression for the dielectric constant to be used in the solution scheme, with an expression which is only slightly more

complex than the conventional one and tends to it when  $\alpha$  tends either to 0 or to 1.

Moreover, if we assume to know  $\phi(\mathbf{r}_1)$  and  $\phi(\mathbf{r}_2)$ , we can derive an interesting expression for the potential located exactly at the intersection with the surface:

$$\begin{aligned} \phi(\mathbf{r}_0) &= (1 - \alpha)\phi(\mathbf{r}_1) + \alpha\phi(\mathbf{r}_2) + (1 - \alpha)ah_v D_{nv} \left( \frac{1}{\varepsilon_2} - \frac{1}{\varepsilon_1} \right) \\ &\approx \phi(\mathbf{r}_1) + \frac{\alpha}{\varepsilon_1} \cdot \frac{\phi(\mathbf{r}_2) - \phi(\mathbf{r}_1)}{\frac{\alpha}{\varepsilon_1} + \frac{(1 - \alpha)}{\varepsilon_2}}. \end{aligned} \quad (31)$$

Expression in Eq. (31) descends from the following approximation:  $D_{nv} \approx D_{nv}^{eff}$ , which becomes true in the  $\varepsilon_2 \gg \varepsilon_1$  limit. Details on its accuracy are deferred to future work. Here, we will benchmark this choice by comparing the surface potential and the ionic energy, which depends on it, against analytical values on single and multiple-sphere systems.

### 3.3. Electrostatic energy calculation

It is convenient now to recast the energy of a linearized Poisson-Boltzmann system as a sum of three terms, as shown in Eq. (9). The Coulombic term, deprived of the singularity related to the self-energy, can be calculated analytically as follows:

$$E_{coul} = \sum_{i=1}^{N_{atoms}} \sum_{j<i} \frac{q_i q_j}{4\pi\varepsilon_m r_{ij}} \quad (32)$$

where  $r_{ij}$  represents the distance between charges  $i$  and  $j$ .

The two remaining energy terms involve surface integrals, and we address them differently.

#### 3.3.1. The polarization contribution

The polarization contribution to the electrostatic energy can be written as the energy of the fixed point charges  $i$  inside the solute subjected to the potential generated by the polarization charges spread over the MS, presented in Eq. (13):

$$E_{pol} = \frac{1}{2} \sum_{i=1}^{N_{atoms}} q_i \int_{\Gamma} \frac{\sigma_{pol}(\tilde{\mathbf{r}})}{4\pi\varepsilon_0 \|\tilde{\mathbf{r}} - \mathbf{r}_i\|} dS \quad (33)$$

where  $\mathbf{r}_i$  is the position of the charge on the  $i$ -th atom and  $\sigma_{pol}$  is the surface polarization charge.

We take advantage of the Gauss law's property to calculate this contribution. In Eq. (29), we conjecture that the best way to approximate a region where there is a dielectric discontinuity with a region where the dielectric is uniform is to assume that the uniform dielectric takes the WHA form. We therefore use  $\mathbf{D}^{eff}$  as the best way to estimate the flux of  $\mathbf{D}_n$  passing through the MS intersected by a cube. Once we have solved the PBE, we can easily derive, for each MS-intersecting edge, the quantity  $D_v^{eff} h_v^2$ , which corresponds to the flux of  $\mathbf{D}^{eff}$  through a square orthogonal to the edge.

If we now consider the flux of  $\mathbf{D}_n$  through the part of the MS contained in the cube, one can note that an accurate evaluation would require a good knowledge of both  $D_n$  and of the local MS shape. But if we apply Gauss law to the space region inside the cube, which is also located between the MS and the square orthogonal to the edge which passes through the intersection, as represented in Fig. 1, we can suggest, since in our model there is no free charge located around the MS, the following approximation:

$$D_{nv} h_v^2 \Big|_{square} \approx \iint_{MS \cap cube} D_n dS. \quad (34)$$

By means of this approach, we derive the total polarization charge  $q_p \approx \varepsilon_0 \left( \frac{1}{\varepsilon_s} - \frac{1}{\varepsilon_m} \right) D_v^{eff} h_v^2$  located on the piece of MS intersecting a

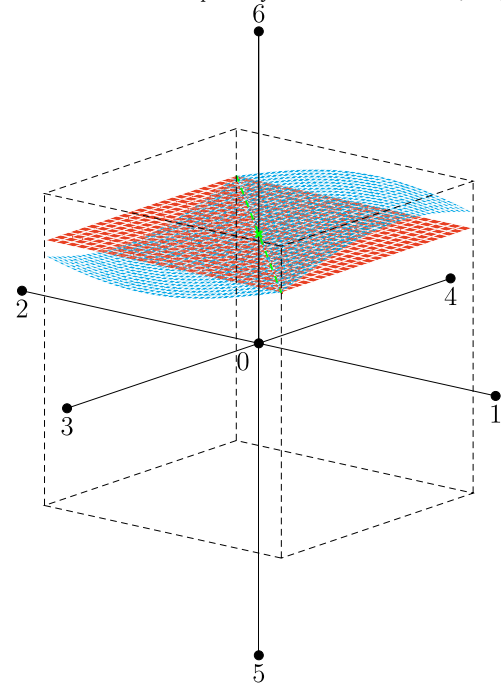


**Fig. 1.** Black dots represent the “current” node 0 and its six adjacent ones. The green cross represents the intersection between the edge connecting nodes 0 and 6 and the MS (in light blue). The reddish square is the intersection between the cube and the plane orthogonal to the edge and passing through the said intersection. The green dashed line represents the intersection between this plane and the MS. (For interpretation of the colors in the figure(s), the reader is referred to the web version of this article.)

cube and concentrate it on the intersection point  $\mathbf{r}_p$  between the MS and the grid. The final calculation takes, therefore, the following form:

$$E_{pol} = \frac{1}{2} \sum_{i=1}^{N_{atoms}} \sum_{p=1}^{N_{Ic}} \frac{q_i q_p}{4\pi\varepsilon_0 \|\mathbf{r}_p - \mathbf{r}_i\|} \quad (35)$$

where  $N_{Ic}$  is the total number of cubes intersecting the MS.

#### 3.3.2. Ionic direct contribution calculation

By considering Eqs. (14) and (9), one can get the expression for the direct ionic contribution:

$$E_{ion} = \frac{1}{2} \sum_{i=1}^{N_{atoms}} q_i \left( \int_{\Gamma} \phi(\tilde{\mathbf{r}}) \frac{(\tilde{\mathbf{r}} - \mathbf{r}_i) \cdot \mathbf{n}(\tilde{\mathbf{r}})}{4\pi \|\tilde{\mathbf{r}} - \mathbf{r}_i\|^3} dS - \frac{1}{\varepsilon_s} \int_{\Gamma} \frac{\mathbf{D}(\tilde{\mathbf{r}}) \cdot \mathbf{n}(\tilde{\mathbf{r}})}{4\pi \|\tilde{\mathbf{r}} - \mathbf{r}_i\|} dS \right). \quad (36)$$

Here, the second integral is equivalent, up to a multiplicative constant, to that in Eq. (33), and thus is treated similarly.

We now focus on discretizing the first integral of Eq. (36):

$$I = \int_{\Gamma} \phi(\tilde{\mathbf{r}}) \frac{(\tilde{\mathbf{r}} - \mathbf{r}_i) \cdot \mathbf{n}(\tilde{\mathbf{r}})}{4\pi \|\tilde{\mathbf{r}} - \mathbf{r}_i\|^3} dS. \quad (37)$$

To evaluate this integral, we take again the advantage of the information delivered by NanoShaper, namely analytical intersections and normals (Fig. 2). This is used to locally re-triangulate the surface via the marching cubes algorithm. The total molecular surface is hence approximated as the union of the triangles:

$$\Gamma \approx \bigcup_{j=1}^{N_t} \Gamma_j \quad (38)$$

where  $N_t$  is the number of triangles in the cube grid. Overall, using this information, the integral (37) can be discretized as follows:

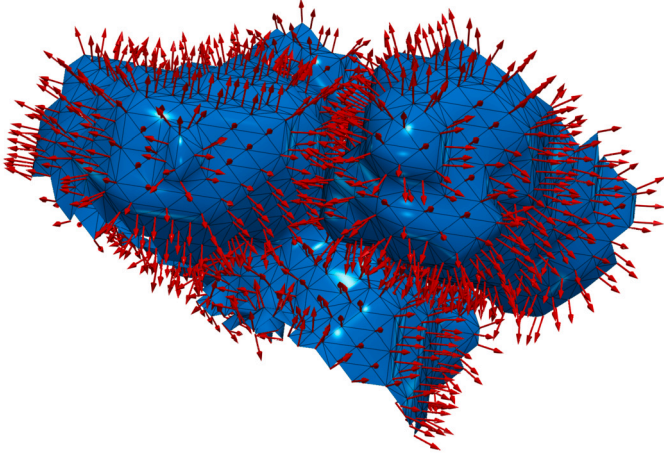


Fig. 2. Triangulation of the MS with normal vectors given by NanoShaper.

$$I \approx \sum_{j=1}^{N_t} \int_{T_j} \phi(\bar{\mathbf{r}}) \frac{(\bar{\mathbf{r}} - \mathbf{r}_i) \cdot \mathbf{n}(\bar{\mathbf{r}})}{4\pi \|\bar{\mathbf{r}} - \mathbf{r}_i\|^3} dS \approx \sum_{j=1}^{N_t} \frac{T_j}{3} \sum_{k=A,B,C} \phi(\mathbf{r}_k) \frac{(\mathbf{r}_k - \mathbf{r}_i) \cdot \mathbf{n}(\mathbf{r}_k)}{4\pi \|\mathbf{r}_k - \mathbf{r}_i\|^3} \quad (39)$$

where  $T_j$  is the area of the  $j$ -th triangle and  $k$  labels its three vertices  $A$ ,  $B$  and  $C$ . The potentials at the triangle vertices are calculated through the formula (31).

While the type of calculations performed in Sect. 2.3 are quite common in the Boundary Element treatment of elliptic PDEs, we are not aware of any Finite Differences or Finite Elements Method-based PB solver implementing this solution for the calculation of the ionic contribution to the electrostatic energy.

### 3.4. Exploiting de-refinement for more efficient BCs

We have shown in Sect. 2.4 that even the likely most accurate BCs used in Finite Difference and Finite Element methods, often called Coulombic, cannot be considered asymptotic, and their accuracy may be sensitive to particular characteristics of the computed system. Furthermore, their computational cost can become significant for large systems, as it involves calculating distance-based functions between all atomic charges and all elements at the boundary of the computational domain where the equation is solved. On the other side, null, homogeneous Dirichlet BCs would, in principle, be exact at a very far distance from the solute regardless of its features, but using a very low percentage filling (aka perfil) could be computationally unfavorable, wasting a lot of computational effort on degrees of freedom located far in the solvent. Let's consider the possibilities given by numerical advances, though. We may note that grid adaptivity, which is usually adopted to increase the accuracy in the most critical regions, which in the PB are the point charges and the MS, can very simply be applied to reduce the resolution in the regions where there are no criticalities. Moreover, while changing resolution near complex geometries may have inherent complexities beyond the simple number of d.o.f., doing this in the solvent is much lighter. This is why we suggest that the overall best trade-off between accuracy and computational cost is to use a uniform grid tight around the system, say with a perfil around 90%, followed by a de-refinement of the grid, until a much lower perfil is reached, say between 15% and 20%. It is worth noting that, due to the specific octree structure of our grid, if we fix the "tight" box size, we can no longer exactly determine the perfil within the entire computational domain. Indeed, the octree structure of cubic elements imposes that the entire computational domain is again a cube having a side length, which is a power of 2 of the inner grid spacing. So, one can only fix an upper bound for the overall perfil.

## 4. Software architecture

The philosophy that guided the design of NextGenPB was, on the one hand, to rely as much as possible on existing Free Software libraries that provide the required capabilities, whenever possible, while, on the other hand, integrating such libraries by means of *adapters* providing an intermediate level of abstraction allowing, when needed, the plug-in addition or replacement of libraries serving similar purposes. This approach is indeed inherited in NextGenPB from its main dependency which is the bimpp C++ library [20,28]. bimpp provides the main methods that implement the distributed memory parallel assembly of the discrete operators discussed in Sect. 3 and, in addition, adapters for parallel solvers for the related linear systems via direct [29,30] or iterative [31,32] methods. While many possible solvers can be invoked through the available interfaces, given the structure of the system derived from the discretization of the linearized PB equation, the most used solver in our tests is the Conjugate Gradient solver implemented in LIS with a SSOR preconditioner so, unless stated otherwise, one can assume that this is the choice adopted for all the tests in the following sections. bimpp also provides a class for managing hierarchically (de)refinable Cartesian Oct-tree meshes, which is essentially a wrapper around the C library p4est [33,34].<sup>1</sup> The description of the molecular surface is handled through an interface to the NanoShaper library which implements a set of different surface description formats [5,12]. Parallel I/O of structured binary data is implemented in bimpp via linking to the liboctave library which is part of GNU Octave [35], so that the output files can be conveniently post processed via scripts using the GNU Octave interpreter; output in vtk file format is also available for visualization.

## 5. An analytical benchmark

For the case of solutes represented by  $N_s$  non-overlapping dielectric spheres  $\Omega_{m,i}$  with the same relative dielectric constant  $\epsilon_{r,m}$  and centered at points  $\mathbf{r}_i \in \mathbb{R}^3$  (each sphere  $\Omega_{m,i}$  is characterized by a radius  $R_i$  and contains a fixed centrally-located point charge  $q_i$ ,  $i = 1, \dots, N_s$ ) we look for the total self-consistent potential  $\phi(\mathbf{r})$  (at a point  $\mathbf{r} \in \mathbb{R}^3$ ) in the form [36,37]

$$\phi(\mathbf{r}) = \begin{cases} \phi_{\text{in},i}(\mathbf{r}) = \phi_{\text{coul},i}(\mathbf{r}) + \check{\phi}_{\text{in},i}(\mathbf{r}), & \mathbf{r} \in \Omega_{m,i}, \\ \phi_{\text{out}}(\mathbf{r}) = \sum_{i=1}^{N_s} \phi_{\text{out},i}(\mathbf{r}), & \mathbf{r} \in \Omega_s, \end{cases} \quad (40)$$

where the sum  $\sum_{i=1}^{N_s} (\cdot)$  in  $\phi_{\text{out}}$  reflects the superposition principle applicable to the Debye-Hückel description. Addend  $\phi_{\text{coul},i}(\mathbf{r}) = \frac{q_i}{4\pi\epsilon_0\epsilon_{r,m}\|\mathbf{r}-\mathbf{r}_i\|}$  in (40) is obviously the Coulombic potential due to the given free charge  $q_i$  situated at  $\mathbf{r}_i$ , while unknown potentials  $\check{\phi}_{\text{in},i}$  and  $\phi_{\text{out},i}$  are expressed through local eigenfunction expansions (of Laplace type for  $\check{\phi}_{\text{in},i}$  and Poisson-Boltzmann type for  $\phi_{\text{out},i}$ )

$$\begin{aligned} \check{\phi}_{\text{in},i}(\mathbf{r}) &= \sum_{n,l} L_{nl,i} \tilde{\sigma}_i^n Y_n^l(\hat{\rho}_i), \\ \phi_{\text{out},i}(\mathbf{r}) &= \sum_{n,l} G_{nl,i} k_n(\tilde{\rho}_i) Y_n^l(\hat{\rho}_i), \end{aligned} \quad (41)$$

where dimensionless  $\tilde{\rho}_i = k_D \rho_i$  is the scaled (by a Debye screening length  $k_D^{-1}$ ) radial coordinate of  $\mathbf{r}$  measured from the  $i$ -th sphere's center (i.e.  $\rho_i = \mathbf{r} - \mathbf{r}_i$ ,  $\rho_i = \|\rho_i\|$ ,  $\hat{\rho}_i = \rho_i/\rho_i$ ),  $k_n(\cdot)$  are modified spherical Bessel functions of the 2nd kind,  $Y_n^l(\cdot)$  are the standard orthonormal complex-valued spherical harmonics (see [38]), and  $\sum_{n,l}(\cdot)$  denotes the sum  $\sum_{n=0}^{+\infty} \sum_{l=-n}^n (\cdot)$ . Unknown coefficients  $L_{nl,i}$  and  $G_{nl,i}$  of (41) are to be determined from boundary conditions on the spheres' boundaries (see details in Appendix D).

<sup>1</sup> While the initial plan was to implement this wrapper as a generic interface allowing for the replacement of p4est with other Octree libraries, the excellent performance of p4est has made the implementation of additional adapters a very low priority task.

According to (40), the total electrostatic energy can now be calculated as  $E = \frac{1}{2} \sum_{i=1}^{N_s} q_i \cdot (\phi_{in,i} - \phi_{coul,i})|_{\phi_i=0} = \frac{1}{2} \sum_{i=1}^{N_s} q_i \cdot \check{\phi}_{in,i}|_{\phi_i=0} = \frac{1}{2} \sum_{i=1}^{N_s} q_i L_{00,i} / \sqrt{4\pi}$  (note that  $Y_0^0 = \frac{1}{\sqrt{4\pi}}$ ); subtracting the Coulombic potential  $\phi_{coul,i}$  from the full potential  $\phi_{in,i}$  (see (40)), to avoid infinity in energy, corresponds to the removal of the so-called self-energy term [14,36].

To deepen the possibilities of comparing calculations based on this analytical model with the results of numerical calculations [14], it is desirable to be able to calculate not only the total electrostatic energy  $E$ , but also its components (see (9)). While the calculation of the Coulombic part is trivial, calculations of other parts become more involved – e.g. in the considered case of centrally located point charges, one can show (see details in Appendix D) that the corresponding resulting reaction potential  $\phi_{pol,i,i}$  at point  $\mathbf{r}_i$  (i.e. at the  $i$ -th sphere's center) created by the total polarization charge density on the  $i$ -th surface ( $\rho_i = R_i$ ) is

$$\phi_{pol,i,i} = \frac{q_i}{4\pi\epsilon_0 R_i} \left( \frac{1}{\epsilon_{r,s}} - \frac{1}{\epsilon_{r,m}} \right), \quad (42)$$

while the potential  $\phi_{pol,i,j}$  created by the same density at point  $\mathbf{r}_j$  (i.e. at the  $j$ -th sphere's center with  $j \neq i$ ) is

$$\phi_{pol,i,j} = \frac{q_i}{4\pi\epsilon_0 a_{ij}} \left( \frac{1}{\epsilon_{r,s}} - \frac{1}{\epsilon_{r,m}} \right) + \left( 1 - \frac{\epsilon_{r,m}}{\epsilon_{r,s}} \right) \sum_{n,l} \frac{n \tilde{R}_i^n L_{n,l,i}}{2n+1} \left( \frac{R_i}{a_{ij}} \right)^{n+1} Y_n^l(\hat{\mathbf{a}}_{ij}), \quad (43)$$

$\tilde{R}_i = k_D R_i$ ,  $\mathbf{a}_{ij} = \mathbf{r}_j - \mathbf{r}_i$  (see Appendix D for details). With the reaction potentials (42) and (43) so obtained one can immediately calculate the corresponding (polarization) energy contributions  $\frac{1}{2} q_i \phi_{pol,i,i}$  and  $\frac{1}{2} q_j \phi_{pol,i,j}$ , for all  $i, j = \overline{1, \dots, N_s}$ ,  $j \neq i$ ; note that  $\frac{1}{2} q_i \phi_{pol,i,i} = \frac{q_i^2}{8\pi\epsilon_0 R_i} \left( \frac{1}{\epsilon_{r,s}} - \frac{1}{\epsilon_{r,m}} \right)$ , which coincides with the conventional Born energy of a single sphere at zero ionic strength (see [36]). Ionic energy contributions (see (9)), as they appear in [14], can then be calculated by subtracting the Coulombic part and the (just derived) polarization contributions from the total energy  $E$ .

We have written MATLAB scripts to calculate the potential and energy using the above analytical expressions ([https://github.com/concept-lab/Analytical\\_Electrostatics/tree/main](https://github.com/concept-lab/Analytical_Electrostatics/tree/main)).

## 6. Results

This section provides a detailed accuracy and computational cost analysis, comparing the proposed PB-solving software with the leading alternatives commonly used in biomolecular simulations. The benchmarks include both analytical solutions and real biomolecular systems. Additionally, we present results on parallelization and scalability obtained using High-Performance Computing (HPC) architectures.

Unless otherwise specified, the following simulations use a solvent dielectric constant of 80, a solute dielectric constant of 2, an ionic strength of 0.145 mol/L and a temperature of 298.15 K.

### 6.1. Accuracy and convergence order

This analysis is made against the finite differences (FD) calculation implemented in the DelPhi [39] software and the second-order accuracy implemented in the MIBPB software [7,40].

#### 6.1.1. Analytically solvable systems

The simplest geometry where the LPBE can be analytically integrated is that having spherical symmetry. In this case, a single dielectric sphere is immersed in an electrolytic solution. Although the spherical system can easily be solved analytically, it shares some commonalities with more complex alternatives since its symmetry differs from that of the

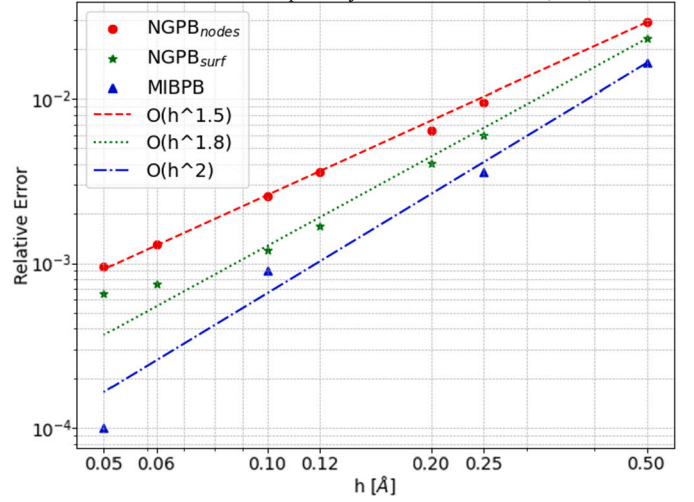


Fig. 3. Convergence order analysis for  $\phi$  in spherical symmetry. The percentage relative error on the electrostatic potential is reported with respect to grid spacing in log-log scale. NGPB exhibits superlinear, 1.5 and 1.8 convergence while MIBPB presents second order accuracy. At a typical resolution of  $h = 0.5 \text{ \AA}$ , the difference in relative percentage error between NGPB and MIBPB is about 1%. The MIBPB results are taken from Ref. [40].

Cartesian grid on which it is mapped and solved. The analytical expressions for the polarization and ion energies are [36, Eq. (88)]:

$$E_{pol} = \frac{1}{2} \left( \frac{1}{\epsilon_s} - \frac{1}{\epsilon_m} \right) \frac{q^2}{4\pi R} \quad (44)$$

$$E_{ion} = -\frac{1}{2} \frac{q^2}{4\pi\epsilon_s} \frac{k_D}{(1 + k_D R)} \quad (45)$$

where  $q$  is the charge,  $R$  is the radius of the sphere, and  $k_D$  is the inverse Debye length.

**Convergence order and accuracy of the potential.** For the analysis of the convergence order on the potential, we reproduced the conditions of the spherical test case (radius = 2 Å, charge of 1 e.s.u.,  $\epsilon_{r,m} = 1$ ,  $\epsilon_{r,s} = 80$ , null ionic strength) of the work of Zhou [40] where the same analysis was performed on the MIBPB software. In that work, the electrostatic potential relative percentage error was considered, as a function of grid resolution. We did the same for NGPB for the potential evaluated exactly at the MS, according to Eq. (31), and for that evaluated at the grid nodes immediately adjacent to the intersections between the grid and the MS. The corresponding results are presented in Fig. 3.

Let us now introduce the ionic contribution in our analysis, we therefore consider now the full model of a Kirkwood sphere, with ionic strength  $I = 0.145 M$ . We use a uniform mesh with a grid spacing of 0.5 Å for all solvers, with 15% of the box filled and homogeneous Dirichlet boundary conditions. This setup removes the effect of boundary conditions from the calculations. We compare the potential at the surface of each solver with that of the analytical solution. In the case of DelPhi and MIBPB, we interpolate the electrostatic potential at any surface point inside a cubic region using the potential values at the eight vertices and employing a trilinear function. The relative errors are represented in box plot format in Fig. 4.

If we compare these accuracy results with the previous ones, we can see that, as already noted in [41], the classical trilinear interpolation may not be the best strategy to estimate a quantity at the point of discontinuity of the constitutive parameter. In contrast, the formula expressed in Eq. (31), seems to be both quite simple and more accurate.

**Convergence order and accuracy of the electrostatic energy.** We analyze now separately the convergence of the different energetic components. Energy is a derived quantity from the potential and its accuracy may

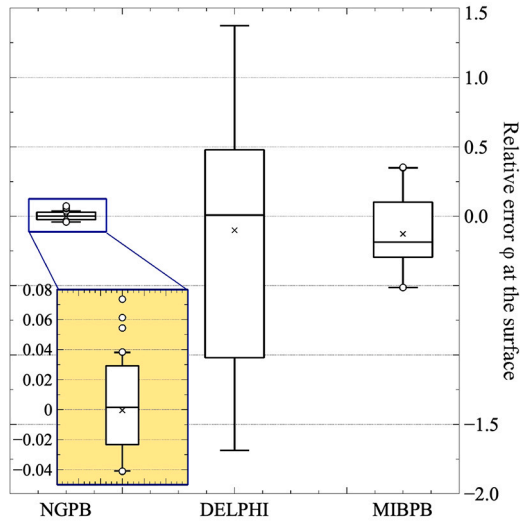


**Fig. 4.** Box plot of signed relative error for the electrostatic potential at the surface compared against analytical results for NGPB, DelPhi and MIBPB for the Kirkwood sphere with  $I=0.145M$ . In box plots, the cross represents the mean of the data, the box represents the interquartile range (IQR), containing the mid 50% of the data, and the whiskers extend to cover 96% of the data. The most extreme 2% on either side are considered outliers.

**Table 1**

Analytical value and signed relative error in energy calculation for NGPB, DelPhi and MIBPB for the Kirkwood sphere. The percentage of box filling is 15%. For MIBPB, we could not identify the energy contributions from the polarization and ionic terms individually, so we report the error for their combined total along with the total energy error.

-	Polarization	Ionic	Total
Value [ $K_b T$ ]	-68.31	-0.35	-68.65
Relative error			
NGPB	7.38e-10	3.39e-02	1.72e-04
DelPhi	5.89e-05	-5.98e-01	-2.97e-03
MIBPB	7.16e-03		7.16e-03

depend on the way how it is calculated. We use again the case of the Kirkwood sphere with  $I=0.145M$  as a benchmark. The overall accuracy is shown in Table 1, the relative error for NGPB is at least one order of magnitude lower than that of the other solvers for each energy term.

The differences in accuracy for the MIBPB code between energy shown here and potential shown in Fig. 3 are consistent with the data shown in the original paper [40], and are not expected to be due to differences in the accuracy of the solution, but rather to how the surface is treated to derive the energy.<sup>2</sup>

For NGPB, we studied separately the convergence order of the polarization and the ionic contributions to energy. Comparable rates are observed for the ionic and total energy errors, as illustrated in Fig. 5. Notably, the polarization energy is extremely accurate already at low resolution. This confirms that the flux method used to calculate the polarization contribution is way more accurate than the method we use to calculate the ionic contribution. Therefore the rate of convergence of the total energy follows that of the latter. It must be also noted, however, that the ionic contribution is smaller than the polarization one, so in absolute terms and unless some specific cancellations occur, as in Table 5, the effect of polarization prevails. It is also worth observing

<sup>2</sup> In the original Ref. [40] the spherical surface was likely described exactly, while in our case, we use the ESES surface builder [42] used in the MIBPB-III software release.

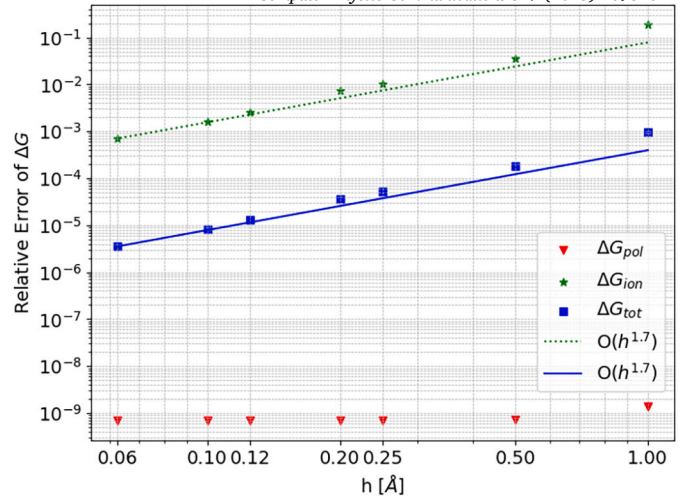


**Fig. 5.** Convergence of the different energy components in NGPB for the Kirkwood sphere. It can be noted that the polarization term, in red, has already reached convergence at the lowest considered scale resolution.

that in the absence of dielectric interfaces or singular sources, linear finite element methods are expected to exhibit quadratic convergence at nodal points, a phenomenon known as superconvergence [20,43]. While the combined effects of discontinuities and point charges in our case prevent the full attainment of this theoretical rate, the NGPB software approaches it closely (order  $\simeq 1.7$ ). This underscores the method's robustness even under non-ideal conditions.

**Non-overlapping spheres.** In the theory exposed in Sect. 5, which has foundations in [36,37,44–46] and in references therein, we showed that it is possible to achieve an analytical solution also for systems composed of many non-overlapping spheres. These systems, which are the many-body evolution of the Kirkwood sphere, pose challenges to the PB solution very similar to real biomolecules, except for what concerns the construction of the MS. For our benchmarking purpose, we select a 30-sphere system, as shown in Fig. 6. The positions of the centers of the 30 spheres are chosen to ensure that the system lacks any symmetry. Additionally, the charges of the atoms in the three spheres with the greatest  $z$ -values are set to zero to evaluate the accuracy of the potential in the center of these atoms, a procedure commonly done in the protocols that estimate the pKa of titratable residues. Also for this benchmark, we assess our code in terms of accuracy and compare it with that of other well-established solvers, such as DelPhi and MIBPB.<sup>3</sup> For all solvers, we use the same grid structure and parameters, a uniform mesh with a grid spacing of  $0.5 \text{ \AA}$ , with 20% of the box filled and homogeneous Dirichlet boundary conditions. No local refinement is adopted despite this feature is available in the NGPB software. Results are presented in Tables 2, 3 and Fig. 7. As in the case of a single sphere, NGPB turns out to be remarkably accurate in calculating both energy and potential at the surface and the atom centers. It is important to note, however, that slight differences in results and accuracy are likely not solely attributable to the equation-solving component, but also to the distinct algorithms used for molecular surface construction and energy calculations, making it difficult to disentangle the respective individual contributions.

**BCs assessment.** We test the proposed approach for the BCs here, which is described in Sect. 3.4. We first show that, as already observed, the BCs and some grid artifacts impact different outputs of the PB solution's outputs differently. Thus, we compare the differences in energies and potentials on a single-sphere system upon application of D-H/Coulombic

<sup>3</sup> It should be noted that none of these PB solvers — including NGPB — have been optimized for systems composed of many non-overlapping spheres.

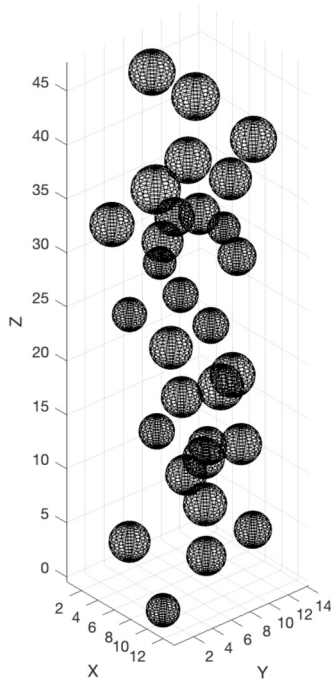


Fig. 6. Schematic representation of 30-spheres system.

Table 2

Analytical value and signed relative error in energy calculation for NGPB, DelPhi and MIBPB on the 30-sphere system. The percentage of box filling is 20%, and null BCs are used. For MIBPB, we can not separate the energy contributions from the polarization and ionic terms individually, so we report the error for their combined total along with the total energy error.

-	Polarization	Ionic	Total
Value [ $K_b T$ ]	-10310.57	-151.13	-2255.59
Relative error			
-	Polarization	Ionic	Total
NGPB	-4.16e-05	1.39e-02	7.46e-04
DelPhi	4.13e-04	-8.85e-02	-4.04e-03
MIBPB	4.00e-03		1.86e-02

Table 3

Signed relative error on uncharged atoms for NGPB, DelPhi and MIBPB on the 30-sphere system. The percentage of box filling is 20% and null BCs are used.

-	Atom1	Atom2	Atom3
NGPB	2.71e-05	-1.19e-03	-4.66e-03
DelPhi	6.04e-04	4.60e-03	8.56e-03
MIBPB	-2.99e-01	-3.07e-01	-2.97e-01

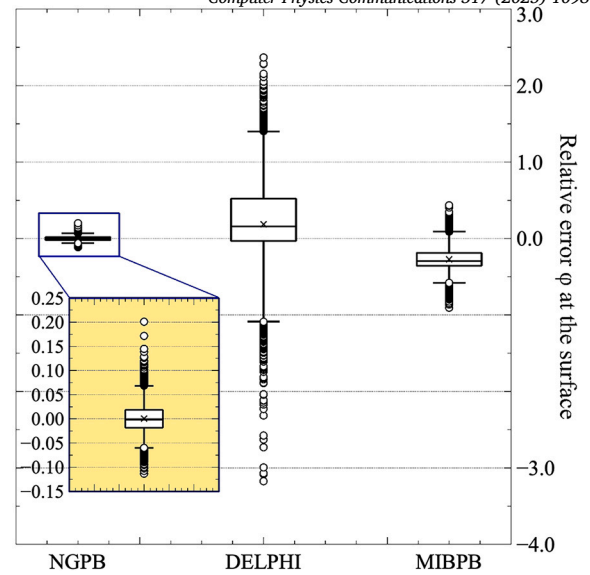


Fig. 7. Box plot of signed relative error of potential at the surface compared with analytical results for NGPB, DelPhi and MIBPB on the 30-sphere system.

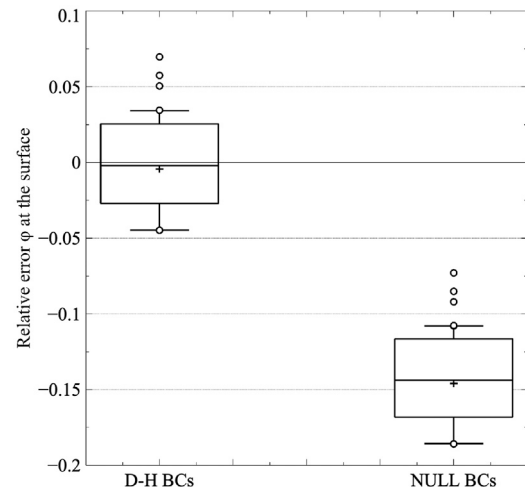


Fig. 8. Box plot of signed relative error of potential at the surface compared with analytical results with NGPB assigning different BCs for one-sphere systems at 80%.

Table 4

Signed relative error in energy calculation with NGPB assigning different BCs for one-sphere systems at 80%.

BCs	Polarization	Ionic	Total
D-H @80%	7.38e-10	4.91e-02	2.49e-04
NULL @80%	7.38e-10	6.12e-01	3.10e-03

BCs wrt null BCs at a perfil of 80%. At this perfil value, the former BCs are far more accurate. However, as it can be seen in Fig. 8 and in Table 4, this difference in accuracy impacts substantially the potential at the surface and, as a consequence, on the ionic energy term, but it goes unnoticed if only the polarization term, which is the most significant, is considered.

We then show the results obtained by leaving a uniform grid resolution on a region of parallelepipedal shape around the solute and performing a grid de-refinement until a much larger computational domain is reached. This technique allows us to bring the boundaries of the computational domain at a distance where null Dirichlet BCs become

accurate irrespective of the system-specific geometry. This is obtained without a significant increment of the number of degrees of freedom, which may even get reduced for highly non-globular solutes relative to standard cubic computational domains (see Fig. 9). For the 30-spheres system, we compare the use of D-H/Coulombic BCs at a perfil of 80% with null BCs, applying de-refinement from 80% to 20% (or smaller) and from 95% to 20% (or smaller). From the results, shown in Fig. 10, we can see excellent results for null BCs when we de-refine until 20% perfil. Moreover, adopting a parallelepipedal rather than cubic uniform grid and possibly going from a perfil of 80%, as commonly done in PB calculations, to that of 95% may compensate for the d.o.f. increment

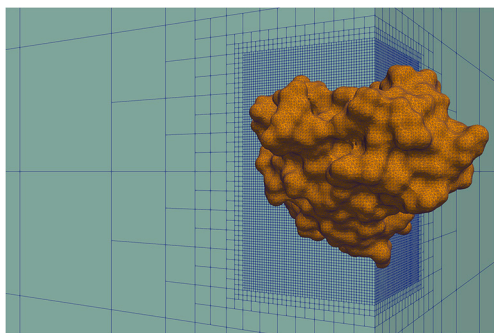


Fig. 9. Representation of the adaptive grid.

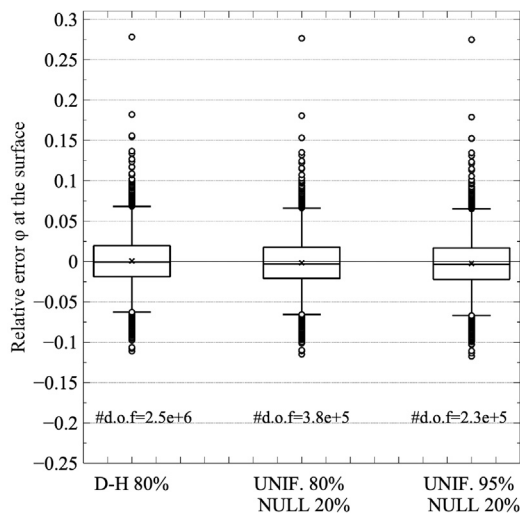


Fig. 10. Box plot of signed relative error of potential at the surface compared with analytical results on the 30-spheres system using different BCs. D-H/Coulombic BCs on a cubic grid with 80% perfil are used in the leftmost column. In the second and third, parallelepipedal uniform grid (perfil of 80% and 95%, respectively) followed by a de-refined one until 20% are used. The reduction in d.o.f. from the first and the second columns is due to the aspect ratio of the system, which permits a further computational saving due to the parallelepipedal shape of the uniform grid.

due to those located in the solvent, in the de-refinement region. Overall, this appears to be a convenient solution in terms of accuracy and computational cost.

## 6.2. Real biomolecular systems

**Electrostatic component of binding energy.** We now assess our computational solution by analyzing its convergence wrt grid resolution on real biomolecular systems. We take six different, representative complexes from the dataset proposed by Fenley and co-workers [47] and observe the convergence of the electrostatic component of the binding free energy ( $\Delta\Delta G^{el}$ ) and the total energy wrt the resolution.  $\Delta\Delta G^{el}$  is calculated as:

$$\Delta\Delta G^{el} = \Delta G_c - \Delta G_1 - \Delta G_2 \quad (46)$$

where  $\Delta G$  is the total electrostatic energy as defined in Eq. (9), and the subscripts  $c$ , 1, and 2 correspond to the complex and the unbound components, respectively (the superscript  $el$  is dropped for simplicity). To measure the convergence rate, we set as reference the results obtained when the grid spacing is 0.2 Å. Moreover, we compare our results with different Poisson-Boltzmann solvers, including CPB [48], MIBPB [40], DelPhi [39], PBSA [49], APBS [50] and FEM-BEM [51], by taking their results from the works [52] and [51].

Table 5

Relative importance of the ionic component wrt  $\Delta\Delta G^{el}$  for each complex.

Complex	Total charge [e]	$\Delta\Delta G_{ion}/\Delta\Delta G$
102d	-20	0.90
227d	-20	1.71
1b27	-4	0.03
1x1x	-3	0.02
1a1t	8	0.59
484d	-16	0.35

We set a 90% perfil uniform grid and de-refine until we reach about the 20% perfil. For each resolution, we randomly displace the solute's centroid 30 times within a cube of half the grid spacing.

In Table 6, we list the mean  $\Delta\Delta G^{el}$  and the total energy, along with their respective standard deviations. Using data for CPB [47] and MIBPB [52], Fig. 11 shows the convergence plots for these solvers alongside those of NGPB. As one can see, we obtained satisfactory convergence at a grid spacing of 0.67 Å for  $\Delta\Delta G^{el}$ . As per the total energy, see Fig. 12, NGPB results are already quite accurate, starting from a grid spacing of 1 Å. For calculating  $\Delta\Delta G^{el}$ , CPB reaches good convergence values for grid spacing values  $\leq 0.4$  Å, while MIBPB has better control over the results at larger spacings and a less rapid convergence in the low spacing range. It is worth noting that both local refinement around the surface, as done in CPB, and second-order accuracy enforcement, as done in MIBPB, entail a quite significant computational cost. The results for individual binding energies at the finest mesh for different solvers (see Fig. 13), also taken from [47,52], are compared with those of NGPB.

Interestingly, while there can be quite significant differences among the results of different solvers and considering that there is no ground truth for these realistic systems, we can however observe that the results of NGPB are always close to those of MIBPB, which is supposedly among the most accurate solvers since it enforces second-order accuracy.<sup>4</sup> It is also important to note that the ionic component of the energy, which is typically negligible compared to other energy components, gains a more significant relative contribution to the binding energy when the systems involved are highly charged. As illustrated in Table 5, we decompose the binding energy into its components, expressed as  $\Delta\Delta G^{el} = \Delta\Delta G_{coul} + \Delta\Delta G_{pol} + \Delta\Delta G_{ion}$ , and examine the relative significance of the ionic component ( $\Delta\Delta G_{ion}$ ) in the total energy. It is plausible that the observed discrepancies among some of the considered solvers, which are larger for more highly charged systems, are due to the specific ways used to calculate this term.

## 6.3. Fixed resolution timings

We want here to provide some information on the timings needed to run the different codes on a number of differently-sized systems. This does not pretend to be an exhaustive analysis, which would need specific tuning of each software and would go beyond the aims of this work, but rather a source of useful information for the reader. We also dedicate a specific section to the treatment of particularly large systems.

**From hundreds to tens of thousands of atoms.** NGPB, MIBPB-III, DelPhi v8.5.0 and APBS v3.4.1 were run on the same machine, an Intel(R) Xeon(R) CPU E5-2620 0 @ 2.00 GHz workstation with RAM: Samsung M393B2G70BH0 - 8 x 16 GB @ 1333 MHz (DIMM DDR3) running Debian GNU/Linux 12. The machine has 12 physical cores, so we present the results for serial running each code and then letting the parallel codes, namely DelPhi and NGPB, exploit the overall number of available cores. It is worth reminding that the considered codes

<sup>4</sup> New results for the complete binding benchmark dataset show excellent agreement between CPB binding energies and those of MIBPB and NGPB (Marcia O. Fenley, private communication).

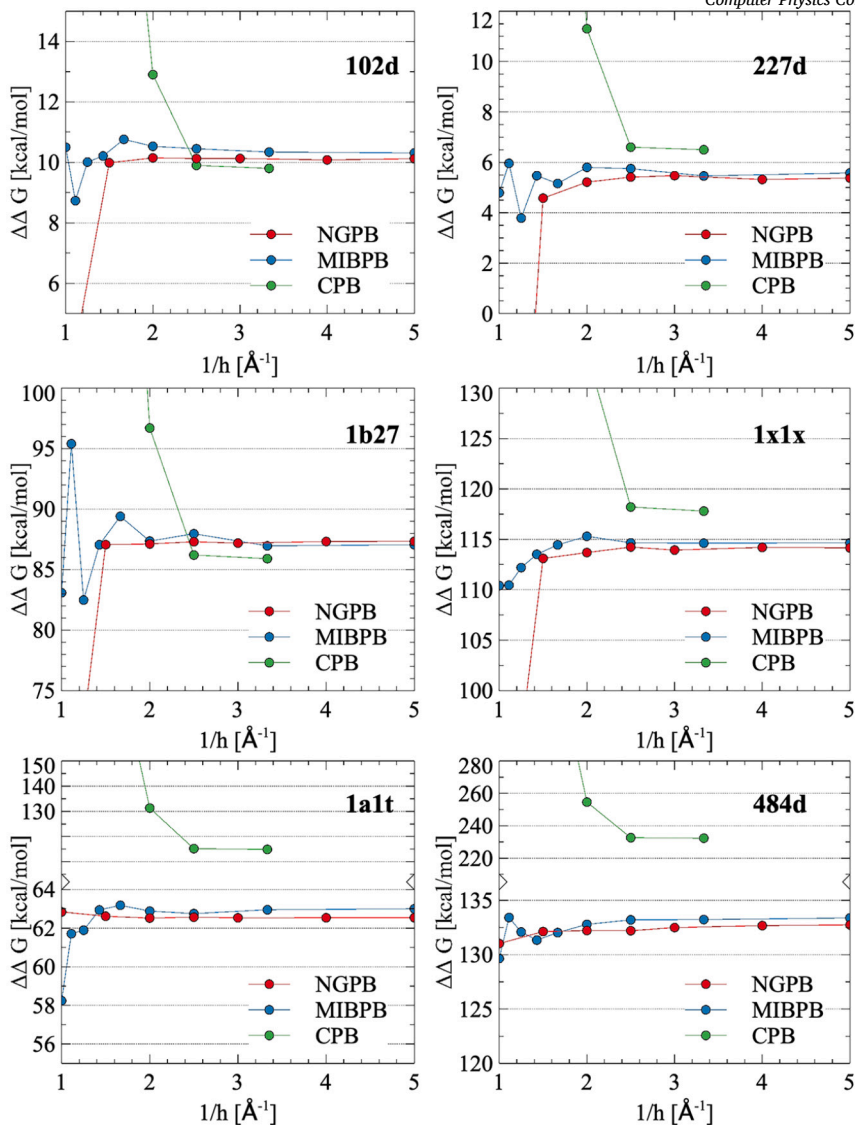


Fig. 11. Convergence trends of  $\Delta\Delta G^{el}$  toward the finest mesh solution, evaluated for NGPB, MIBPB, and CPB approaches. (Online version in colour.)

have different ways of building the grids, which might greatly impact on computational cost and timing. We divided the benchmark set in two subsets: *small\_to\_medium*, containing systems already described in Sect. 6.2, which cover a range of size from about 800 to 3200 atoms, and *large*, containing different numbers of chains of the first crystal structure of the human adenovirus, pdb code 1VSZ (now superseded by 4CWU), which cover the range from about 14000 to about 60000 atoms. On the first set we test MIBPB, DelPhi, NGPB and APBS, while on the second, we only test the parallel codes, that is DelPhi and NGPB. The choice of the resolution is not obvious, in Fig. 14, we present results where all the calculations are performed with the typical resolution used for biomolecular systems, that is  $h = 0.5 \text{ \AA}$ . In the Supplementary Material, we also try a different approach, similarly to what was done in the work of Zhou et al. [40], where the time performance was considered while keeping fixed accuracy.

Boundary conditions are MDH for MIBPB and APBS, so-called Coulombic for DelPhi with 80% of percentage filling, and as described in Sect. 3.4 for NGPB. As one can see, the performance of the parallel version of NextGenPB is remarkably good and not much impacted by the inclusion of the ionic contribution into the calculations. It is worth reminding that our estimate of the timing for ionic contribution calculation for DelPhi and APBS consists in running the code twice, with two different ionic strength values. At fixed resolution, for the smallest sys-

tems and when the ionic contribution is neglected, the DelPhi code is faster than NGPB, probably due to its matrix-free approach.

*From hundreds of thousands to millions of atoms.* The most recent experimental techniques are providing us with structures at atomic or near-atomic resolution of unprecedented size. The computational challenges in solving such large systems' electrostatics are not trivial. Here, NGPB was challenged to calculate the electrostatic potential of the human adenovirus structure and of the swine virus H1N1 capsid. These calculations were run on a cluster of 25 nodes featuring AMD EPYC 7413 CPUs and 512 GB of RAM. The resulting electrostatic potential and field lines deriving from the calculation of the entire 1VSZ system (180457 atoms) are shown in Fig. 15. For the H1N1 system, having more than 14M atoms,<sup>5</sup> a grid spacing of  $h = 1.3 \text{ \AA}$  and an experimental, memory parsimonious, version of NanoShaper were used. The resulting electrostatic potential was plotted on the molecular surface calculated with NanoShaper, providing visual insights into the charge distribution and potential binding hotspots, as illustrated in Fig. 16.

<sup>5</sup> For sake of precision, after removal of the hydrogen atoms, 6.5M atoms remained.

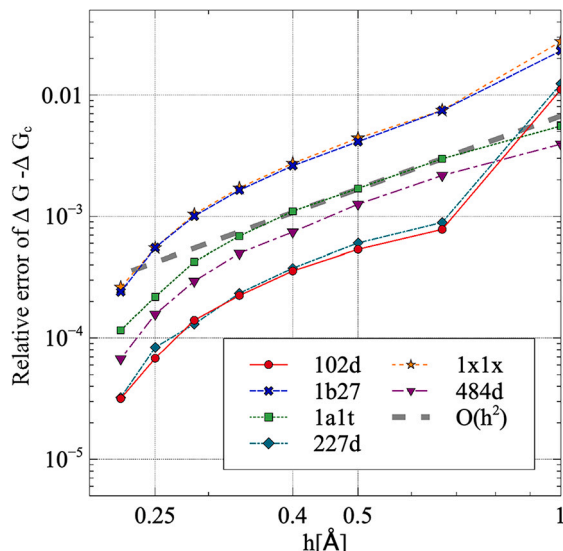


Fig. 12. NGPB convergence profile for the polarization and ionic contributions to the electrostatic energy, corresponding to the total minus the analytically calculable Coulombic term, w.r.t. the case where  $h = 0.2 \text{ \AA}$ .

**Table 6**  
Convergence results for electrostatic free energies and  $\Delta\Delta G$ .

h [Å]	102d		1b27		1a1t	
	$\Delta\Delta G$	$\sigma$	$\Delta\Delta G$	$\sigma$	$\Delta\Delta G$	$\sigma$
1.00	11.16	28.10	54.49	12.44	63.17	2.30
0.67	9.87	1.34	86.71	2.41	62.82	1.09
0.50	10.01	0.42	87.16	0.99	62.35	0.68
0.40	10.24	0.43	87.31	0.72	62.79	0.50
0.33	10.08	0.42	87.34	0.34	62.54	0.26
0.25	10.08	0.28	87.30	0.22	62.51	0.23
0.20	10.08	0.20	87.35	0.17	62.59	0.19
h [Å]	$\Delta G$	$\sigma$	$\Delta G$	$\sigma$	$\Delta G$	$\sigma$
1.00	-25612.73	21.94	-64947.35	6.20	-41003.42	1.92
0.67	-25550.94	1.13	-64982.73	1.49	-41012.02	0.80
0.50	-25552.22	0.34	-64990.27	0.79	-41016.33	0.37
0.40	-25553.14	0.29	-64993.69	0.43	-41018.32	0.29
0.33	-25553.83	0.30	-64995.87	0.19	-41019.71	0.11
0.25	-25554.65	0.18	-64998.33	0.13	-41021.29	0.15
0.20	-25555.00	0.14	-64999.58	0.08	-41022.01	0.09
h [Å]	227d		1x1x		484d	
	$\Delta\Delta G$	$\sigma$	$\Delta\Delta G$	$\sigma$	$\Delta\Delta G$	$\sigma$
1.00	-17.30	26.39	74.41	13.91	130.84	4.09
0.67	4.58	1.82	112.77	1.84	131.93	0.93
0.50	5.43	1.02	113.87	0.89	132.16	0.57
0.40	5.43	0.53	114.12	0.63	132.00	0.52
0.33	5.43	0.27	114.05	0.51	132.37	0.46
0.25	5.47	0.25	114.09	0.44	132.60	0.30
0.20	5.38	0.18	114.19	0.22	132.63	0.30
h [Å]	$\Delta G$	$\sigma$	$\Delta G$	$\sigma$	$\Delta G$	$\sigma$
1.00	-27099.69	22.64	-64663.93	5.28	-39427.15	2.91
0.67	-27030.78	1.43	-64707.76	1.08	-39435.01	0.66
0.50	-27032.26	0.45	-64714.43	0.61	-39439.08	0.48
0.40	-27033.44	0.35	-64718.07	0.59	-39441.38	0.34
0.33	-27034.18	0.18	-64720.31	0.44	-39442.46	0.24
0.25	-27034.96	0.18	-64722.83	0.268	-39443.98	0.18
0.20	-27035.40	0.14	-64724.03	0.17	-39444.68	0.09

## 7. Discussion and conclusions

Here we present a new solving and analyzing framework for the Poisson-Boltzmann equation where we leverage the availability of a very accurate description of the molecular surface, as provided by the NanoShaper software, by employing some analytical derivations that

are used to customize the Cartesian FEM used to discretize and then solve the equation. The analytical contributions and corrections were used to make the expressions of the stiffness and mass matrices more accurate and to accelerate the calculation of the different components of the solvated system's electrostatic energy.

Interestingly, we also constructed an analytical benchmark consisting of combinations of non-overlapping spheres where numerical PB methods can be challenged. The availability of analytical results concerning more realistic systems is of paramount importance for making educated assessments of the solvers' quality.

On the numerical side, we use a Cartesian grid that can be locally refined, if needed. In our experience, however, the best trade-off between accuracy and computational cost for biomolecular systems consists of adopting a uniform grid of  $h = 0.5 \text{ \AA}$ , tightly enclosing the system, and de-refining it (via de-duplication) until a global percentage of filling between 15 and 20% is reached. At the boundaries of the larger domain, homogeneous Dirichlet boundary conditions are applied. Together with our treatment of the dielectric discontinuity, this allows a good quality determination of the different energy contributions and surface potential while limiting the overall number of degrees of freedom and, therefore, the overall computational cost.

Our analysis corroborates that, when calculated via the electric displacement flux method, the polarization energy term is quite robust concerning grid artifacts and boundary condition accuracy. In contrast, the estimated value of the potential at the surface and, by consequence, that of the ionic contribution are more sensitive to both aspects.

We validate our new approach first against the ground truth represented by our analytical expressions, which, by separately providing the different energy terms, allow for a detailed analysis of the accuracy of the results and convergence order. Then, we consider real biomolecular systems for which no analytical expression is available. Our figure of merit, in this case, is the rate of convergence of the total energy wrt grid resolution for different relative mutual placements wrt the grid. We use existing simulation data to compare our performance with that of some widely used codes.

Overall, the performance of NextGenPB is remarkable: in terms of accuracy, it reproduces analytically-derived electrostatic potentials at the molecular surface and energies with a relative error which is at least one order of magnitude smaller than that of the considered alternatives at the same grid resolution. This results both from the accuracy of the calculated potential on the grid and from our potential interpolation approach at the molecular surface. On realistic systems, it quickly converges to the target value, and it yields results very close to those of MIBPB, which is expected to be the most accurate alternative since it enforces second-order accuracy. Interestingly, the capability to accurately calculate the ionic contribution allowed highlighting its relevance in estimating the  $\Delta\Delta G$ . Indeed, while the ionic contribution is a small fraction of the others in the  $\Delta G$ , it can become prominent, due to cancellations of the other terms, if the systems are highly charged, as it occurs with nucleic acids, when the  $\Delta\Delta G$  are derived.

In regard to computational efficiency, the better description of the dielectric discontinuity at almost no cost allows for better accuracy without the need to perform local refinements or second-order accuracy enforcement, which are computationally costly. Moreover, the derivation of the ionic contribution as an integral over the molecular surface allows its separate determination in only one run, in contrast to what is often done by other approaches, where two runs at different ionic strengths are required. Finally, using grid de-refinement to impose null Dirichlet boundary conditions at a large distance from the solute allows saving the calculation of D-H-like ones without compromising on accuracy and while still keeping limited the overall number of degrees of freedom.

Under these considerations, the proposed approach, which marries analytical calculations and established numerical approaches, proves to achieve noteworthy cost-effectiveness. It paves the way for accurate and accelerated derivations of electrostatic potentials on large datasets

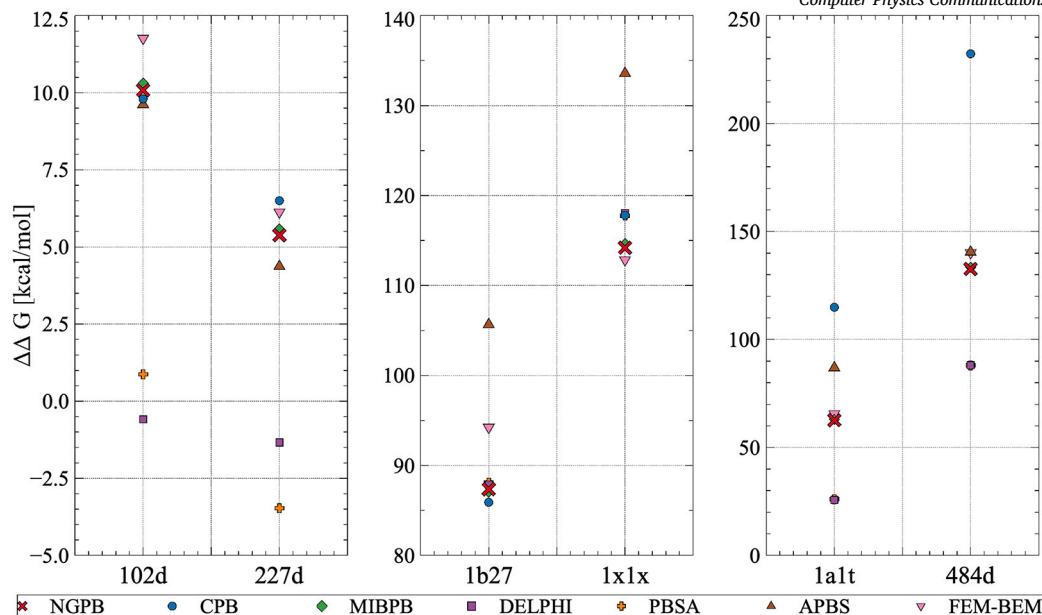


Fig. 13. Binding energies for different solvers at 0.2 Å grid spacing.

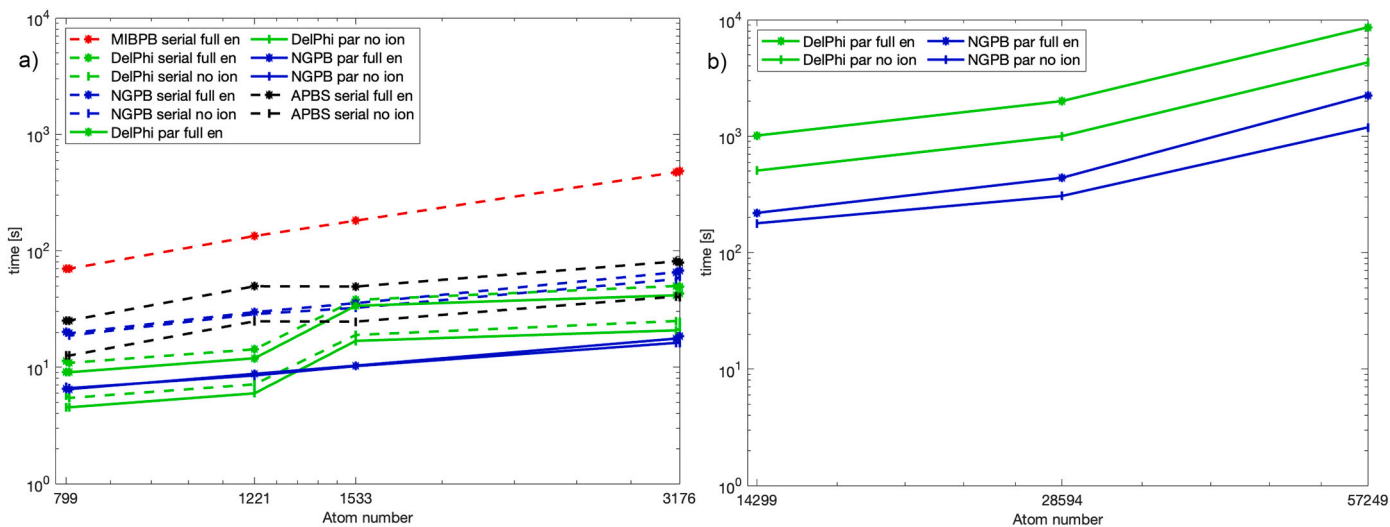
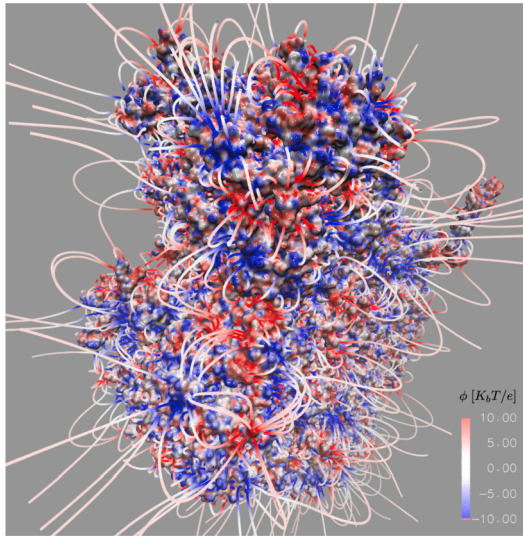


Fig. 14. Timing plot for different codes at fixed scale ( $h = 0.5 \text{ \AA}$ ). a) Loglog graphic of timings for MIBPB (in red), DelPhi (in green), NGPB (in blue), and APBS (in black). Dashed lines correspond to serial versions, whereas solid lines describe parallel runs. Stars indicate full energy calculations (Coulombic + Polarization + Ionic contribution) while vertical ticks point to calculations where ionic contribution is neglected, as often done. For the DelPhi and APBS codes, the ionic contribution is calculated by running the code twice, at different values of ionic strength. The systems are those described in Sect. 6.2 (having 799, 805, 1221, 1533, 3154, and 3176 atoms). b) Loglog graphic for the timings obtained by the parallel codes, that is DelPhi and NGPB, on larger systems, obtained by pruning the 1VSZ structure (14299, 28594, and 57249 atoms). (Online version in colour.)

that can be used to feed, for instance, machine learning tools. A prototypical version of NGPB was incorporated in the MCCE software to describe the protonation states of proteins [10], which yielded auspicious results. The future outlook for this activity is to transfer as many as possible of these improvements to a full nonlinear PB solver. Moreover, we are working on letting NGPB inherit the ability of NanoShaper to automatically filter out the internal cavities that are smaller than a given threshold in volume, in order to give the users the freedom to decide where they want the high-dielectric constant to be assigned to. As a general comment, it is conceivable that the approach of using local analytical solutions in the elements crossing a sharp boundary can be profitably applied to other PDEs. Indeed, models leading to finite discontinuities in the constitutive parameters are relatively common in many fields, for instance, in models generated via Computer-Assisted Design.

#### CRediT authorship contribution statement

**Vincenzo Di Florio:** Writing – review & editing, Writing – original draft, Visualization, Validation, Software, Methodology, Data curation. **Patrizio Ansalone:** Validation, Supervision, Formal analysis, Conceptualization. **Sergii V. Siryk:** Writing – review & editing, Writing – original draft, Validation, Supervision, Software, Methodology, Formal analysis. **Sergio Decherchi:** Writing – review & editing, Software, Data curation. **Carlo de Falco:** Writing – review & editing, Writing – original draft, Validation, Supervision, Software, Resources, Project administration, Methodology, Investigation, Funding acquisition, Formal analysis, Conceptualization. **Walter Rocchia:** Writing – review & editing, Writing – original draft, Validation, Supervision, Software, Resources, Project administration, Methodology, Investigation, Funding acquisition, Formal analysis, Conceptualization.



**Fig. 15.** Human adenovirus structure (pdb id 1VSZ, 180457 atoms) with the molecular surface colored based on the local electrostatic potential calculated by NGPB and showing main electric field lines.

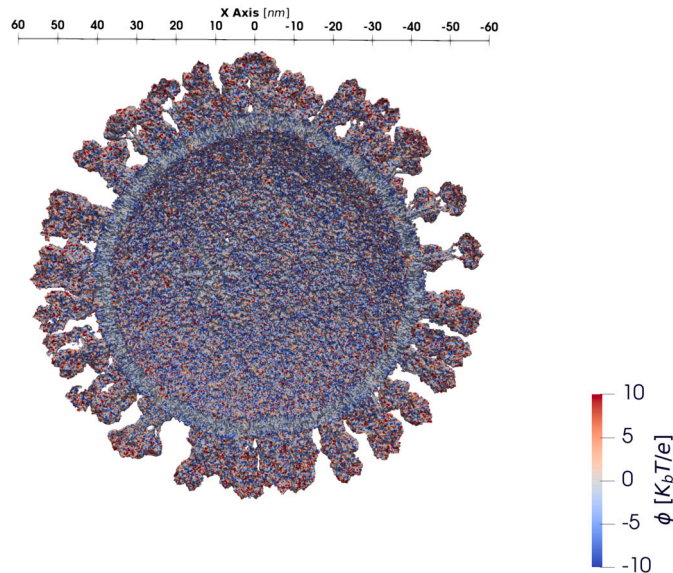


**Fig. 16.** Cross section of the H1N1 swine virus structure, having the molecular surface colored based on the local electrostatic potential.

#### Declaration of competing interest

The authors declare that they have no known competing financial interests or personal relationships that could have appeared to influence the work reported in this paper.

#### Acknowledgements

We acknowledge the financial support from the European Union - NextGenerationEU and the Ministry of University and Research (MUR), National Recovery and Resilience Plan (NRRP): Research program CN00000013 “National Centre for HPC, Big Data and Quantum Computing”, CUP: J33C22001180001, funded by the D.D. n. 1031, 17.06.2022 and Mission 4, Component 2, Investment 1.4 - Avviso “Centri Nazionali” - D.D. n. 3138, 16 December 2021; and PNRR MUR Project PE0000013 “Future Artificial Intelligence Research (FAIR)”, CUP: J53C22003010006.

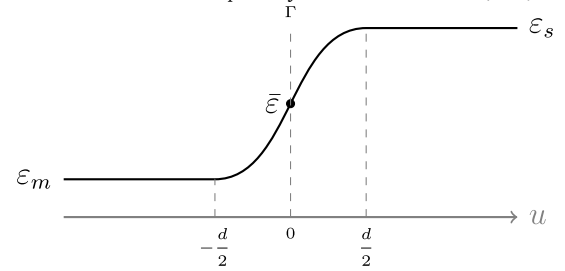


**Fig. A.17.** Schematic representation of the approximated variation of  $\epsilon$ .

The simulations discussed in this work have been performed on the HPC Cluster of the Department of Mathematics of Politecnico di Milano which was funded by MUR grant Dipartimenti di Eccellenza 2023-2027, on the Franklin supercomputer of IIT, and on the CINECA supercomputers, thanks to EUROHPC and ISCR initiatives.

The authors would like to thank Prof. C. Burstedde for fruitful discussion about the implementation of an efficient algorithm for depositing point charges on octree grids. They thank also Prof. M. O. Fenley for discussing the analysis of the results, and Dr. J. Chen, for providing a MIBPB code compatible with our machine allowing us to perform our tests.

A special thanks goes to Martina Politi, whose master thesis at Politecnico di Milano [53] provided the first proof-of-concept for the development of NextGenPB.

C. de Falco is a member of the Gruppo Nazionale Calcolo Scientifico-Istituto Nazionale di Alta Matematica (GNCS-INdAM).

V. Di Florio is a member of Gruppo Nazionale di Fisica Matematica (GNFM) of Istituto Nazionale di Alta Matematica (INdAM).

#### Appendix A. Application of Green’s identities to partition the internal potential

Let’s write Eq. (7) in operatorial form:

$$L[\phi] = \rho^f, \quad (\text{A.1})$$

where the linear operator  $L$  is defined as:

$$L = -\nabla \cdot (\epsilon(\mathbf{r})\nabla(\cdot)) + c(\mathbf{r})(\cdot) \quad \mathbf{r} \in D. \quad (\text{A.2})$$

A straightforward application of the second Green’s identity to the operator  $L$  is not possible, since  $\epsilon(\mathbf{r})$  is not continuous and, consequently, the electrostatic potential is not differentiable at the surface  $\Gamma$ . Therefore, we will attempt a non rigorous derivation, where the gradient of  $\epsilon$  is considered in a distributional sense. More in detail, we consider  $\epsilon(\mathbf{r})$ , which is a step function with the discontinuity located on  $\Gamma$ , as a limit for  $d \rightarrow 0^+$  of the following function:

$$\epsilon_d(\mathbf{r}) = \frac{\epsilon_s - \epsilon_m}{2} \left[ \operatorname{erf} \left( \frac{u(\mathbf{r})}{d} \right) + 1 \right] + \epsilon_m. \quad (\text{A.3})$$

For the definition of  $u$ , we start by considering for each  $\mathbf{r}$  near the surface, its orthogonal projection on  $\Gamma$ , namely  $\mathbf{r}_\Gamma \in \Gamma$ , and its direction  $\mathbf{n}(\mathbf{r}_\Gamma)$ . We define  $u$  as the oriented distance from the surface itself:  $u(\mathbf{r}) = (\mathbf{r} - \mathbf{r}_\Gamma) \cdot \mathbf{n}(\mathbf{r}_\Gamma)$ . In this approximation,  $\epsilon_d(u=0) = \bar{\epsilon} = \frac{\epsilon_m + \epsilon_s}{2}$ . A schematic general representation of  $\epsilon_d$  is shown in Fig. A.17. It is interesting to note that numerical FEM-BEM-coupled modeling with MS represented as a continuous interface (similarly to (A.3) with non-zero  $d$ ) and the corresponding impact of such diffused interfaces on solvation and binding energy, were very recently treated in [54]. In addition to the error function erf, the work [54] has benchmarked other sigmoidal functions (like tanh) to couple the internal and external regions.

Let’s now consider the gradient of  $\epsilon_d$ , it is aligned with the normal at the surface and takes the following form:

$$\nabla \epsilon_d(\mathbf{r}) = \frac{d\epsilon_d(u)}{du} \nabla u = (\epsilon_s - \epsilon_m) \mathcal{N}(0, \frac{d^2}{2}) \mathbf{n}(\mathbf{r}_\Gamma) \quad (\text{A.4})$$

(here the symbol  $\mathcal{N}(0, d^2/2)$  indicates the normal distribution density function with zero mean and variance  $d^2/2$ ).

In the  $d \rightarrow 0$  limit, we obtain the gradient expression:

$$\nabla \varepsilon(\mathbf{r}) = (\varepsilon_s - \varepsilon_m) \delta(\mathbf{r} - \mathbf{r}_\Gamma) \cdot \mathbf{n}(\mathbf{r}_\Gamma) \mathbf{n}(\mathbf{r}_\Gamma) \quad \mathbf{r}_\Gamma \in \Gamma. \quad (\text{A.5})$$

In what follows, we assume that the limits for  $d \rightarrow 0^+$  and the integral operators can be swapped. Similarly to what is done in the case of the second Green's identity, we consider the following identity:

$$\int_{\Omega} \{L[v]w - L[w]v\} dV = \int_{\Omega} \nabla \cdot [\varepsilon(v \nabla w - w \nabla v)] dV \quad (\text{A.6})$$

where  $\Omega \subseteq D$ ,  $w$  and  $v$  are suitable test functions,  $\bar{\mathbf{r}}$  is the integration variable.

Let us now instantiate Eq. (A.6) by choosing  $\Omega = \Omega_m$ ,  $w(\bar{\mathbf{r}}) = \phi(\bar{\mathbf{r}})$  as the solution of Eq. (A.1), and  $v(\bar{\mathbf{r}}) = \frac{q}{4\pi\varepsilon_m \|\bar{\mathbf{r}} - \mathbf{r}\|}$  representing the point charge potential centered at the observation point  $\mathbf{r} \in \Omega_m$ . The left-hand side (LHS) of Eq. (A.6) then takes on the following form:

$$\int_{\Omega_m} \{L[v(\bar{\mathbf{r}})]\phi(\bar{\mathbf{r}}) - L[\phi(\bar{\mathbf{r}})]v(\bar{\mathbf{r}})\} dV = \int_{\Omega_m} \left\{ q\phi(\bar{\mathbf{r}}) \left[ \frac{c(\bar{\mathbf{r}})}{4\pi\varepsilon_m \|\bar{\mathbf{r}} - \mathbf{r}\|} + \frac{\varepsilon(\bar{\mathbf{r}})}{\varepsilon_m} \delta(\bar{\mathbf{r}} - \mathbf{r}) + \frac{\nabla(\varepsilon(\bar{\mathbf{r}})) \cdot (\bar{\mathbf{r}} - \mathbf{r})}{4\pi\varepsilon_m \|\bar{\mathbf{r}} - \mathbf{r}\|^3} \right] - \frac{\rho^f q}{4\pi\varepsilon_m \|\bar{\mathbf{r}} - \mathbf{r}\|} \right\} dV. \quad (\text{A.7})$$

In  $\Omega_m$ ,  $c(\bar{\mathbf{r}}) = 0$  and  $\varepsilon(\mathbf{r}) = \varepsilon_m$ . Relation (A.7) then becomes:

$$\begin{aligned} & \int_{\Omega_m} \{L[v(\bar{\mathbf{r}})]\phi(\bar{\mathbf{r}}) - L[\phi(\bar{\mathbf{r}})]v(\bar{\mathbf{r}})\} dV = \\ & = q\phi(\mathbf{r}) + \frac{q}{4\pi\varepsilon_m} \int_{\Omega_m} \phi(\bar{\mathbf{r}}) \frac{\nabla(\varepsilon(\bar{\mathbf{r}})) \cdot (\bar{\mathbf{r}} - \mathbf{r})}{\|\bar{\mathbf{r}} - \mathbf{r}\|^3} dV - \frac{q}{4\pi\varepsilon_m} \int_{\Omega_m} \frac{\rho^f}{\|\bar{\mathbf{r}} - \mathbf{r}\|} dV = \\ & = q\phi(\mathbf{r}) + \frac{q}{4\pi\varepsilon_m} \int_{\Omega_m} \phi(\bar{\mathbf{r}}) (\varepsilon_s - \varepsilon_m) \frac{\delta((\bar{\mathbf{r}} - \bar{\mathbf{r}}_\Gamma) \cdot \mathbf{n}(\bar{\mathbf{r}}_\Gamma)) \mathbf{n}(\bar{\mathbf{r}}_\Gamma) \cdot (\bar{\mathbf{r}} - \mathbf{r})}{\|\bar{\mathbf{r}} - \mathbf{r}\|^3} dV + \\ & \quad - \frac{q}{4\pi\varepsilon_m} \int_{\Omega_m} \frac{\rho^f}{\|\bar{\mathbf{r}} - \mathbf{r}\|} dV. \end{aligned} \quad (\text{A.8})$$

Thanks to the *single layer* property of the Dirac delta function and considering that, along the limit for  $d \rightarrow 0$  process, we are integrating only on the internal half of the layer enclosing the surface where  $\varepsilon_d$  is changing, we can recast the following volume integral in a surface one:

$$\begin{aligned} & \int_{\Omega_m} \phi(\bar{\mathbf{r}}) (\varepsilon_s - \varepsilon_m) \frac{\delta((\bar{\mathbf{r}} - \bar{\mathbf{r}}_\Gamma) \cdot \mathbf{n}(\bar{\mathbf{r}}_\Gamma)) \mathbf{n}(\bar{\mathbf{r}}_\Gamma) \cdot (\bar{\mathbf{r}} - \mathbf{r})}{\|\bar{\mathbf{r}} - \mathbf{r}\|^3} dV = \\ & = \frac{\varepsilon_s - \varepsilon_m}{2} \int_{\partial\Omega_m} \phi(\bar{\mathbf{r}}) \frac{(\bar{\mathbf{r}} - \mathbf{r}) \cdot \mathbf{n}(\bar{\mathbf{r}})}{\|\bar{\mathbf{r}} - \mathbf{r}\|^3} dS. \end{aligned} \quad (\text{A.9})$$

In the present case,  $\partial\Omega_m \equiv \Gamma$  and  $\mathbf{n}$  denotes the unit vector orthogonal to  $\Gamma$  and oriented in the outward direction.

Let us now consider the RHS of (A.6) in our instantiation:

$$\begin{aligned} & \int_{\Omega_m} \nabla \cdot [\varepsilon(\bar{\mathbf{r}})v(\bar{\mathbf{r}})\nabla\phi(\bar{\mathbf{r}}) - \varepsilon(\bar{\mathbf{r}})\phi(\bar{\mathbf{r}})\nabla v(\bar{\mathbf{r}})] dV = \\ & = - \int_{\Omega_m} \nabla \cdot [v(\bar{\mathbf{r}})\mathbf{D}(\bar{\mathbf{r}})] dV + \int_{\Omega_m} \nabla \cdot \left[ \varepsilon(\bar{\mathbf{r}})\phi(\bar{\mathbf{r}}) \frac{q(\bar{\mathbf{r}} - \mathbf{r})}{4\pi\varepsilon_m \|\bar{\mathbf{r}} - \mathbf{r}\|^3} \right] dV = \\ & = -q \int_{\Gamma} \frac{\mathbf{D}(\bar{\mathbf{r}}) \cdot \mathbf{n}(\bar{\mathbf{r}})}{4\pi\varepsilon_m \|\bar{\mathbf{r}} - \mathbf{r}\|} dS + q \int_{\Gamma} \bar{\varepsilon}\phi(\bar{\mathbf{r}}) \frac{(\bar{\mathbf{r}} - \mathbf{r}) \cdot \mathbf{n}(\bar{\mathbf{r}})}{4\pi\varepsilon_m \|\bar{\mathbf{r}} - \mathbf{r}\|^3} dS, \end{aligned} \quad (\text{A.10})$$

where  $\mathbf{D}$  is the electric displacement vector and  $(\nabla \cdot)_n = \nabla(\cdot) \cdot \mathbf{n}$ . The application of the divergence theorem done in this latest derivations was a bit more natural in the integral involving  $\mathbf{D}$  since its normal component is continuous, while the contribution to the integral given by the discontinuous tangential component is nullified by the scalar product with  $\mathbf{n}$ . In the second integral, in contrast, we have been forced to consider the limit of  $\varepsilon_d$ . Combining (A.8) and (A.10), we can express the electrostatic potential in any point of  $\Omega_m$  as follows:

$$\begin{aligned} \phi(\mathbf{r}) & = \int_{\Omega_m} \frac{\rho^f}{4\pi\varepsilon_m \|\bar{\mathbf{r}} - \mathbf{r}\|} dV - \frac{\varepsilon_s - \varepsilon_m}{2} \int_{\Gamma} \phi(\bar{\mathbf{r}}) \frac{(\bar{\mathbf{r}} - \mathbf{r}) \cdot \mathbf{n}(\bar{\mathbf{r}})}{4\pi\varepsilon_m \|\bar{\mathbf{r}} - \mathbf{r}\|^3} dS + \\ & \quad - \int_{\Gamma} \frac{\mathbf{D}(\bar{\mathbf{r}}) \cdot \mathbf{n}(\bar{\mathbf{r}})}{4\pi\varepsilon_m \|\bar{\mathbf{r}} - \mathbf{r}\|} dS + \int_{\Gamma} \bar{\varepsilon}\phi(\bar{\mathbf{r}}) \frac{(\bar{\mathbf{r}} - \mathbf{r}) \cdot \mathbf{n}(\bar{\mathbf{r}})}{4\pi\varepsilon_m \|\bar{\mathbf{r}} - \mathbf{r}\|^3} dS = \\ & = \int_{\Omega_m} \frac{\rho^f}{4\pi\varepsilon_m \|\bar{\mathbf{r}} - \mathbf{r}\|} dV - \int_{\Gamma} \frac{\mathbf{D}(\bar{\mathbf{r}}) \cdot \mathbf{n}(\bar{\mathbf{r}})}{4\pi\varepsilon_m \|\bar{\mathbf{r}} - \mathbf{r}\|} dS + \\ & \quad + \int_{\Gamma} \phi(\bar{\mathbf{r}}) \frac{(\bar{\mathbf{r}} - \mathbf{r}) \cdot \mathbf{n}(\bar{\mathbf{r}})}{4\pi \|\bar{\mathbf{r}} - \mathbf{r}\|^3} dS, \end{aligned}$$

which actually yields Eq. (10).

## Appendix B. Ionic potential: from volume to surface formulation

If we repeat the previous calculations by assuming  $\Omega = \Omega_s$ , and therefore accounting for the fact that in this region  $\rho^f(\bar{\mathbf{r}}) = 0$  while  $c(\bar{\mathbf{r}}) \neq 0$  (except for the Stern layer, if any), and by choosing as test function  $v(\bar{\mathbf{r}}) = \frac{q}{4\pi\varepsilon_s \|\bar{\mathbf{r}} - \mathbf{r}\|}$ , with  $\mathbf{r} \in \Omega_m$ , we obtain, for the LHS of Eq. (A.6):

$$\begin{aligned} & \int_{\Omega_s} \{L[v(\bar{\mathbf{r}})]\phi(\bar{\mathbf{r}}) - L[\phi(\bar{\mathbf{r}})]v(\bar{\mathbf{r}})\} dV = \\ & = \int_{\Omega_s} q\phi(\bar{\mathbf{r}}) \left[ \frac{c(\bar{\mathbf{r}})}{4\pi\varepsilon_s \|\bar{\mathbf{r}} - \mathbf{r}\|} + \frac{\nabla\varepsilon(\bar{\mathbf{r}}) \cdot (\bar{\mathbf{r}} - \mathbf{r})}{\|\bar{\mathbf{r}} - \mathbf{r}\|^3} \right] dV, \end{aligned} \quad (\text{B.1})$$

and for its RHS:

$$\begin{aligned} & \int_{\Omega_s} \nabla \cdot [\varepsilon(\bar{\mathbf{r}})v(\bar{\mathbf{r}})\nabla\phi(\bar{\mathbf{r}}) - \varepsilon(\bar{\mathbf{r}})\phi(\bar{\mathbf{r}})\nabla v(\bar{\mathbf{r}})] dV = \\ & = -q \int_{\Gamma \cup \Sigma} \frac{\mathbf{D}(\bar{\mathbf{r}}) \cdot \mathbf{m}(\bar{\mathbf{r}})}{4\pi\varepsilon_s \|\bar{\mathbf{r}} - \mathbf{r}\|} dS + q \int_{\Gamma \cup \Sigma} \bar{\varepsilon}'\phi(\bar{\mathbf{r}}) \frac{(\bar{\mathbf{r}} - \mathbf{r}) \cdot \mathbf{m}(\bar{\mathbf{r}})}{4\pi\varepsilon_s \|\bar{\mathbf{r}} - \mathbf{r}\|^3} dS, \end{aligned} \quad (\text{B.2})$$

where  $\bar{\varepsilon}' = \bar{\varepsilon}$  on  $\Gamma$  and  $\bar{\varepsilon}' = \varepsilon_s$  on  $\Sigma$ , and  $\mathbf{m}$  is the outward normal from  $\Omega_s$ ;  $\Gamma$  is the surface separating  $\Omega_s$  from  $\Omega_m$  and  $\Sigma$  is the external surface enclosing  $\Omega_s$ . If, as it is commonly assumed, the solvent region extends to infinity, it can be shown that the surface integrals over  $\Sigma$  vanish. Consistently, the normal vector  $\mathbf{m}$  on  $\Gamma$  coincides with  $-\mathbf{n}$ . If we now equate Eqs. (B.1) and (B.2), and consider that  $\rho^s(\bar{\mathbf{r}}) = -c(\bar{\mathbf{r}})\phi(\bar{\mathbf{r}})$ , we get:

$$\int_{\Omega_s} \frac{\rho^s(\bar{\mathbf{r}})}{4\pi\varepsilon_s \|\bar{\mathbf{r}} - \mathbf{r}\|} dV = - \int_{\Gamma} \frac{\mathbf{D}(\bar{\mathbf{r}}) \cdot \mathbf{n}(\bar{\mathbf{r}})}{4\pi\varepsilon_s \|\bar{\mathbf{r}} - \mathbf{r}\|} dS + \int_{\Gamma} \phi(\bar{\mathbf{r}}) \frac{(\bar{\mathbf{r}} - \mathbf{r}) \cdot \mathbf{n}(\bar{\mathbf{r}})}{4\pi \|\bar{\mathbf{r}} - \mathbf{r}\|^3} dS. \quad (\text{B.3})$$

It is interesting to note that the LHS of the latter equation is the potential generated by the ions in solution screened by the polarizable solvent, evaluated at a point  $\mathbf{r}$  inside the solute. This is the exact definition of the reaction potential coming from the ions in solution, that we call  $\phi_{ion}$  (see (14) and (9)). We get here a direct derivation of what has been found at the end of Sect. 2.3.

### Appendix C. Application of Green's identities to partition the potential in the solvent

There is a third way to apply the same procedure seen in the two previous Appendices, to extract further interesting information. In this case, we again assume  $\Omega = \Omega_s$ , and account for the fact that in this region  $\rho^f(\bar{\mathbf{r}}) = 0$  while  $c(\bar{\mathbf{r}}) \neq 0$  (except that in the Stern layer, if any). In contrast to the previous applications, we choose as test function the D-H solution for a single charge in solution, with the observer location  $\mathbf{r} \in \Omega_s$ :

$$v(\bar{\mathbf{r}}) = \frac{qe^{-k_D\|\bar{\mathbf{r}}-\mathbf{r}\|}}{4\pi\epsilon_s\|\bar{\mathbf{r}}-\mathbf{r}\|}. \quad (\text{C.1})$$

To simplify the derivation, we assume the distance of  $\mathbf{r}$  from the surface  $\Gamma$  is larger than any  $d$  considered in the limiting process for  $\epsilon_d$  (see Appendix A), so that we can always assume that  $\epsilon(\mathbf{r}) = \epsilon_s$ . The LHS of Eq. (A.6) yields

$$\begin{aligned} & \int_{\Omega_s} \{L[v(\bar{\mathbf{r}})]\phi(\bar{\mathbf{r}}) - L[\phi(\bar{\mathbf{r}})]v(\bar{\mathbf{r}})\} dV = \\ & = -q \int_{\text{Stern layer}} \phi(\bar{\mathbf{r}}) \frac{k_D^2 e^{-k_D\|\bar{\mathbf{r}}-\mathbf{r}\|}}{4\pi\|\bar{\mathbf{r}}-\mathbf{r}\|} dV + \\ & + q \int_{\Omega_s} \phi(\bar{\mathbf{r}}) \frac{\nabla\epsilon(\bar{\mathbf{r}}) \cdot (\bar{\mathbf{r}}-\mathbf{r}) e^{-k_D\|\bar{\mathbf{r}}-\mathbf{r}\|} (1+k_D\|\bar{\mathbf{r}}-\mathbf{r}\|)}{4\pi\epsilon_s\|\bar{\mathbf{r}}-\mathbf{r}\|^3} dV + q\phi(\mathbf{r}), \end{aligned} \quad (\text{C.2})$$

where the term  $q\phi(\mathbf{r})$  results from the convolution of  $\phi(\bar{\mathbf{r}})$  with the Dirac delta arising from the PB operator, while the RHS of Eq. (A.6) yields:

$$\begin{aligned} & \int_{\Omega_s} \nabla \cdot [\epsilon(\bar{\mathbf{r}})v(\bar{\mathbf{r}})\nabla\phi(\bar{\mathbf{r}}) - \epsilon(\bar{\mathbf{r}})\phi(\bar{\mathbf{r}})\nabla v(\bar{\mathbf{r}})] dV = \\ & = -q \int_{\Gamma \cup \Sigma} \frac{e^{-k_D\|\bar{\mathbf{r}}-\mathbf{r}\|} \mathbf{D}(\bar{\mathbf{r}}) \cdot \mathbf{m}(\bar{\mathbf{r}})}{4\pi\epsilon_s\|\bar{\mathbf{r}}-\mathbf{r}\|} dS + \\ & + q \int_{\Gamma \cup \Sigma} \bar{\epsilon}'\phi(\bar{\mathbf{r}}) \frac{e^{-k_D\|\bar{\mathbf{r}}-\mathbf{r}\|} (1+k_D\|\bar{\mathbf{r}}-\mathbf{r}\|)(\bar{\mathbf{r}}-\mathbf{r}) \cdot \mathbf{m}(\bar{\mathbf{r}})}{4\pi\epsilon_s\|\bar{\mathbf{r}}-\mathbf{r}\|^3} dS, \end{aligned} \quad (\text{C.3})$$

where  $\bar{\epsilon}' = \bar{\epsilon}$  on  $\Gamma$  and  $\bar{\epsilon}' = \epsilon_s$  on  $\Sigma$ ,  $\mathbf{m}$  is the outward normal from  $\Omega_s$ ,  $\Gamma$  is the surface separating  $\Omega_s$  from  $\Omega_m$  and  $\Sigma$  is the external surface enclosing  $\Omega_s$ . If, as it is commonly assumed, the solvent region extends to infinity, it can be shown that the surface integrals over  $\Sigma$  vanish. Consistently, the normal vector  $\mathbf{m}$  on  $\Gamma$  coincides with  $-\mathbf{n}$ . If we now equate Eqs. (C.2) and (C.3) and reorder the terms, we will finally get:

$$\begin{aligned} \phi(\mathbf{r}) = & \int_{\text{Stern layer}} \phi(\bar{\mathbf{r}}) \frac{k_D^2 e^{-k_D\|\bar{\mathbf{r}}-\mathbf{r}\|}}{4\pi\|\bar{\mathbf{r}}-\mathbf{r}\|} dV + \int_{\Gamma} \frac{e^{-k_D\|\bar{\mathbf{r}}-\mathbf{r}\|} \mathbf{D}(\bar{\mathbf{r}}) \cdot \mathbf{n}(\bar{\mathbf{r}})}{4\pi\epsilon_s\|\bar{\mathbf{r}}-\mathbf{r}\|} dS + \\ & - \int_{\Gamma} \phi(\bar{\mathbf{r}}) \frac{e^{-k_D\|\bar{\mathbf{r}}-\mathbf{r}\|} (1+k_D\|\bar{\mathbf{r}}-\mathbf{r}\|)(\bar{\mathbf{r}}-\mathbf{r}) \cdot \mathbf{n}(\bar{\mathbf{r}})}{4\pi\|\bar{\mathbf{r}}-\mathbf{r}\|^3} dS, \end{aligned} \quad (\text{C.4})$$

which actually yields Eq. (15).

### Appendix D. Details on analytical calculations done in Sect. 5

Unknown coefficients  $L_{nl,i}$  and  $G_{nl,i}$  of (41) are to be determined from boundary conditions on the boundaries of spheres – namely,

$$\begin{aligned} \phi_{\text{in},i} \Big|_{o_i \rightarrow R_i^-} &= \phi_{\text{out}} \Big|_{o_i \rightarrow R_i^+}, \\ \epsilon_{r,m} (\hat{\mathbf{n}}_i \cdot \nabla \phi_{\text{in},i}) \Big|_{o_i \rightarrow R_i^-} &= \epsilon_{r,s} (\hat{\mathbf{n}}_i \cdot \nabla \phi_{\text{out}}) \Big|_{o_i \rightarrow R_i^+}, \end{aligned} \quad (\text{D.1})$$

where  $\hat{\mathbf{n}}_i$  is the outer unit normal on the boundary of  $\Omega_{m,i}$ . When imposing boundary conditions (D.1) on the  $i$ -th spherical surface,

to have all quantities represented through the same basis functions set (namely, spherical harmonics  $\{Y_n^l(\hat{\rho}_i)\}_{0 \leq |l| \leq n}$ ), we expand the off-side (i.e. those with respect to center  $\mathbf{r}_j$ ,  $j \neq i$ ) screened harmonics  $\{k_n(\tilde{\rho}_j)Y_n^l(\hat{\rho}_j)\}_{0 \leq |l| \leq n}$  in  $\phi_{\text{out}}$  using relations (see [44,45])  $k_L(\tilde{\rho}_j)Y_L^M(\hat{\rho}_j) = \sum_{l_1, m_1} \mathcal{H}_{l_1, m_1}^{LM}(\mathbf{a}_{ij})_{l_1}(\tilde{\rho}_j)Y_{l_1}^{m_1}(\hat{\rho}_j)$  with coefficients

$$\mathcal{H}_{l_1, m_1}^{LM}(\mathbf{a}_{ij}) = \sum_{l_2, m_2} (-1)^{l_1+l_2} H_{l_1, m_1, l_2, m_2}^{LM} k_{l_2}(\tilde{a}_{ij}) Y_{l_2}^{m_2}(\hat{\mathbf{a}}_{ij}) \quad \text{and}$$

$$H_{l_1, m_1, l_2, m_2}^{LM} = C_{l_1, 0, l_2, 0}^{L0} C_{l_1, m_1, l_2, m_2}^{LM} \sqrt{\frac{4\pi(2l_1+1)(2l_2+1)}{2L+1}},$$

where  $\mathbf{a}_{ij} = \mathbf{r}_j - \mathbf{r}_i$  points from  $\mathbf{r}_i$  to  $\mathbf{r}_j$ ,  $\rho_i < a_{ij} = \|\mathbf{a}_{ij}\|$ ,  $\tilde{a}_{ij} = k_D a_{ij}$ ,  $C_{l_1, m_1, l_2, m_2}^{LM} = \langle l_1 l_2; m_1 m_2 | LM \rangle$  are Clebsch-Gordan coefficients,  $i_n(\cdot)$  are modified spherical Bessel functions of the 1st kind. Doing so, we, in particular, ensure the correct mathematical treatment of mutual polarization effects [36]. These operations readily convert boundary conditions (D.1) into a linear algebraic system governing the unknown coefficients of (41); by solving it [36], unknown potentials (41) are thereby completely determined. Note that in practical numerical calculations, in a manner completely similar to the particular case of 2-sphere systems extensively described in [36], one needs to limit index  $n$  in (41) (and this then naturally impacts the size of the linear system formed) by some user-defined threshold  $n_{\text{max}}$ , i.e. one has  $0 \leq n \leq n_{\text{max}}$  everywhere in the calculations; now gradually increasing  $n_{\text{max}}$  one ensures that potentials and/or other monitored quantities (such as energy) stop changing (their changes become negligible and not affecting the data within the precision reported in the work).

In order to establish equality (42) we observe that the total polarization charge density at the  $i$ -th surface ( $o_i = R_i$ ) is [36]

$$\begin{aligned} \sigma_{\text{tot},i}(\hat{\rho}_i) &= \epsilon_0 \left( \frac{1}{\epsilon_{r,m}} - \frac{1}{\epsilon_{r,s}} \right) \epsilon_{r,m} k_D \frac{\partial}{\partial \hat{\rho}_i} \phi_{\text{in},i} \Big|_{o_i=R_i} \\ &= \epsilon_0 \left( \frac{1}{\epsilon_{r,m}} - \frac{1}{\epsilon_{r,s}} \right) \epsilon_{r,m} k_D \left( \frac{-q_i k_D}{4\pi\epsilon_0\epsilon_{r,m}\hat{\rho}_i^2} + \sum_{n,l} L_{nl,i} n \hat{\rho}_i^{n-1} Y_n^l(\hat{\rho}_i) \right) \Big|_{o_i=R_i}, \end{aligned}$$

so that the corresponding resulting reaction potential  $\phi_{\text{pol},i,i}$  created by this density at point  $\mathbf{r}_i$  (the  $i$ -th sphere's center) is thus expressed by integral over the surface  $\partial\Omega_{m,i}$  of sphere  $\Omega_{m,i}$  (note the orthogonality property of spherical harmonics when integrating them over sphere):

$$\phi_{\text{pol},i,i} = \frac{1}{4\pi\epsilon_0} \oint_{\partial\Omega_{m,i}} \frac{\sigma_{\text{tot},i}(\hat{\rho}_i)}{R_i} dS = \frac{q_i}{4\pi\epsilon_0 R_i} \left( \frac{1}{\epsilon_{r,s}} - \frac{1}{\epsilon_{r,m}} \right),$$

that is equality (42).

Next, in order to establish equality (43), i.e. to evaluate the resulting potential  $\phi_{\text{pol},i,j} = \frac{1}{4\pi\epsilon_0} \oint_{\partial\Omega_{m,i}} \frac{\sigma_{\text{tot},i}(\hat{\rho}_i) dS}{\|\mathbf{R}_i \hat{\rho}_i - \mathbf{a}_{ij}\|}$  created by density  $\sigma_{\text{tot},i}$  at point  $\mathbf{r}_j$  (note that  $\mathbf{R}_i \hat{\rho}_i - \mathbf{a}_{ij}$  is the vector,  $\rho_j$ , pointing from  $\mathbf{r}_j$  to the integration point on  $\partial\Omega_{m,i}$  corresponding to  $\mathbf{R}_i \hat{\rho}_i$ ) let us use the addition theorem for spherical harmonics (see [38, §3.6]) to express

$$\frac{1}{\|\mathbf{R}_i \hat{\rho}_i - \mathbf{a}_{ij}\|} = \frac{4\pi}{a_{ij}} \sum_{n,l} \frac{1}{2n+1} \left( \frac{R_i}{a_{ij}} \right)^n Y_n^l(\hat{\mathbf{a}}_{ij}) Y_n^l(\hat{\rho}_i)^*,$$

from which taking into account the orthogonality property of spherical harmonics one then readily obtains relation (43).

### Appendix E. Supplementary material

Supplementary material related to this article can be found online at <https://doi.org/10.1016/j.cpc.2025.109816>.

### Data availability

Code and data are made available at a link in the manuscript.

## References

- [1] W. Yang, W. Rocchia, Biomolecular electrostatic phenomena: an evergreen field, *J. Phys. Chem. B* 127 (18) (2023) 3979–3981, PMID: 37165646, <https://doi.org/10.1021/acs.jpcc.3c02158>.
- [2] E. Besley, Recent developments in the methods and applications of electrostatic theory, *Acc. Chem. Res.* 56 (17) (2023) 2267–2277, PMID: 37585560, <https://doi.org/10.1021/acs.accounts.3c00068>.
- [3] R. Blossy, *The Poisson-Boltzmann Equation*, Springer International Publishing, Cham, 2023, pp. 1–25.
- [4] S. Decherchi, J. Colmenares, C.E. Catalano, M. Spagnuolo, E. Alexov, W. Rocchia, Between algorithm and model: different molecular surface definitions for the Poisson-Boltzmann based electrostatic characterization of biomolecules in solution, *Commun. Comput. Phys.* 13 (1) (2013) 61–89, <https://doi.org/10.4208/cicp.050711.111111s>.
- [5] S. Decherchi, W. Rocchia, A general and robust ray-casting-based algorithm for triangulating surfaces at the nanoscale, *PLoS ONE* 8 (4) (2013) 1–15, <https://doi.org/10.1371/journal.pone.0059744>.
- [6] R. Rohs, S.M. West, A. Sosinsky, P. Liu, R.S. Mann, B. Honig, The role of DNA shape in protein–DNA recognition, *Nature* 461 (7268) (2009) 1248–1253, <https://doi.org/10.1038/nature08473>.
- [7] D. Chen, Z. Chen, C. Chen, W. Geng, G.-W. Wei, MIBPB: a software package for electrostatic analysis, *J. Comput. Chem.* 32 (4) (2011) 756–770, <https://doi.org/10.1002/jcc.21646>, <https://onlinelibrary.wiley.com/doi/abs/10.1002/jcc.21646>.
- [8] J. Iwahara, B.M. Pettitt, B. Yu, Direct measurements of biomolecular electrostatics through experiments, *Curr. Opin. Struct. Biol.* 82 (2023) 102680.
- [9] B. Yu, X. Wang, J. Iwahara, Measuring local electrostatic potentials around nucleic acids by paramagnetic NMR spectroscopy, *J. Phys. Chem. Lett.* 13 (42) (2022) 10025–10029.
- [10] Y. Song, J. Mao, M.R. Gunner, MCCE2: improving protein pKa calculations with extensive side chain rotamer sampling, *J. Comput. Chem.* 30 (14) (2009) 2231–2247, <https://doi.org/10.1002/jcc.21222>, <https://onlinelibrary.wiley.com/doi/abs/10.1002/jcc.21222>.
- [11] M. Machuqueiro, A.M. Baptista, Constant-pH molecular dynamics with ionic strength effects: protonation-conformation coupling in decalysine, *J. Phys. Chem. B* 110 (6) (2006) 2927–2933, PMID: 16471903, <https://doi.org/10.1021/jp056456q>.
- [12] S. Decherchi, A. Spitaleri, J. Stone, W. Rocchia, NanoShaper–VMD interface: computing and visualizing surfaces, pockets and channels in molecular systems, *Bioinformatics* 35 (7) (2018) 1241–1243, <https://doi.org/10.1093/bioinformatics/bty761>.
- [13] K.A. Sharp, B. Honig, Calculating total electrostatic energies with the nonlinear Poisson-Boltzmann equation, *J. Phys. Chem.* 94 (19) (1990) 7684–7692.
- [14] W. Rocchia, E. Alexov, B. Honig, Extending the applicability of the nonlinear Poisson-Boltzmann equation: multiple dielectric constants and multivalent ions, *J. Phys. Chem. B* 105 (28) (2001) 6507–6514.
- [15] W. Rocchia, Poisson-Boltzmann equation boundary conditions for biological applications, in: *Modelling Complex Systems in Molecular Biology and Tumor Dynamics and Control*, *Math. Comput. Model.* 41 (10) (2005) 1109–1118, <https://doi.org/10.1016/j.mcm.2005.05.006>, <https://www.sciencedirect.com/science/article/pii/S089571770500169X>.
- [16] D.S. Malkus, T.J. Hughes, Mixed finite element methods – reduced and selective integration techniques: a unification of concepts, *Comput. Methods Appl. Mech. Eng.* 15 (1) (1978) 63–81.
- [17] J. Roberts, J.-M. Thomas, Mixed and hybrid methods, in: *Finite Element Methods (Part 1)*, in: *Handbook of Numerical Analysis*, vol. 2, Elsevier, 1991, pp. 523–639, <https://www.sciencedirect.com/science/article/pii/S1570865905800419>.
- [18] T.H. Robey, The primal mixed finite element method and the LBB condition, *Numer. Methods Partial Differ. Equ.* 8 (4) (1992) 357–379, <https://doi.org/10.1002/num.1690080405>, <https://onlinelibrary.wiley.com/doi/pdf/10.1002/num.1690080405>.
- [19] O.C. Zienkiewicz, R.L. Taylor, J.Z. Zhu, *The Finite Element Method*, vol. 1, Butterworth-Heinemann, Oxford, UK, 2013.
- [20] P.C. Africa, C. de Falco, S. Perotto, Scalable recovery-based adaptation on Cartesian quadtree meshes for advection-diffusion-reaction problems, *Adv. Comput. Sci. Eng.* 1 (4) (2023) 443–473, <https://doi.org/10.3934/acse.2023018>, <https://www.aims-science.org/article/id/6589317592d3ad47ddcab725>.
- [21] F. Gatti, M. Fois, C. de Falco, S. Perotto, L. Formaggia, Parallel simulations for fast-moving landscapes: space-time mesh adaptation and sharp tracking of the wetting front, *Int. J. Numer. Methods Fluids* 95 (8) (2023) 1286–1309, <https://doi.org/10.1002/flid.5186>, <https://onlinelibrary.wiley.com/doi/pdf/10.1002/flid.5186>.
- [22] D. Boffi, F. Brezzi, M. Fortin, *Algebraic Aspects of Saddle Point Problems*, Springer Berlin Heidelberg, Berlin, Heidelberg, 2013, pp. 123–195.
- [23] J.-C. Nédélec, Mixed finite elements in  $\mathbb{R}^3$ , *Numer. Math.* 35 (1980) 315–341.
- [24] J.-C. Nédélec, A new family of mixed finite elements in  $\mathbb{R}^3$ , *Numer. Math.* 50 (1986) 57–81.
- [25] O.C. Zienkiewicz, R.L. Taylor, P. Nithiarasu, J. Zhu, *The Finite Element Method*, vol. 3, McGraw-Hill, 1977.
- [26] J. Xu, L. Zikatanov, A monotone finite element scheme for convection-diffusion equations, *Math. Comput.* 68 (228) (1999) 1429–1446.
- [27] P.A. Markowich, M.A. Zlámal, Inverse-average-type finite element discretizations of selfadjoint second-order elliptic problems, *Math. Comput.* 51 (184) (1988) 431–449.
- [28] C. de Falco, bimpp, <https://www.github.com/bimpp>. (Accessed 23 December 2024).
- [29] P. Amestoy, I. Duff, J.-Y. L'Excellent, Multifrontal parallel distributed symmetric and unsymmetric solvers, *Comput. Methods Appl. Mech. Eng.* 184 (2) (2000) 501–520, [https://doi.org/10.1016/S0045-7825\(99\)00242-X](https://doi.org/10.1016/S0045-7825(99)00242-X), <https://www.sciencedirect.com/science/article/pii/S004578259900242X>.
- [30] C. Burstedde, L.C. Wilcox, T. Isaac, MUMPS: multifrontal massively parallel sparse direct solver, <https://www.p4est.org>. (Accessed 10 December 2024).
- [31] A. Nishida, Experience in developing an open source scalable software infrastructure in Japan, in: D. Taniar, O. Gervasi, B. Murgante, E. Pardede, B.O. Apduhan (Eds.), *Computational Science and Its Applications – ICCSA 2010*, Springer Berlin Heidelberg, Berlin, Heidelberg, 2010, pp. 448–462.
- [32] A. Nishida, Lis: library of iterative solvers for linear systems, <https://www.ssisic.org/lis>. (Accessed 10 December 2024).
- [33] C. Burstedde, L.C. Wilcox, O. Ghattas, p4est: scalable algorithms for parallel adaptive mesh refinement on forests of octrees, *SIAM J. Sci. Comput.* 33 (3) (2011) 1103–1133, <https://doi.org/10.1137/100791634>.
- [34] C. Burstedde, L.C. Wilcox, T. Isaac, p4est: parallel AMR on forests of octrees, <https://www.p4est.org>. (Accessed 10 December 2024).
- [35] J.W. Eaton, D. Bateman, S. Hauberg, R. Wehbring, GNU Octave version 9.2.0 manual: a high-level interactive language for numerical computations, <https://www.gnu.org/software/octave/doc/v9.2.0/>, 2024.
- [36] S.V. Siryk, A. Bendandi, A. Diaspro, W. Rocchia, Charged dielectric spheres interacting in electrolytic solution: a linearized Poisson-Boltzmann equation model, *J. Chem. Phys.* 155 (2021) 114114.
- [37] S. Siryk, W. Rocchia, Arbitrary-shape dielectric particles interacting in the linearized Poisson-Boltzmann framework: an analytical treatment, *J. Phys. Chem. B* 126 (2022) 10400–10426.
- [38] J.D. Jackson, *Classical Electrodynamics*, 3rd edition, John Wiley & Sons Ltd, London, Sydney, Singapore, New York, 1999.
- [39] L. Li, C. Li, S. Sarkar, J. Zhang, S. Witham, Z. Zhang, L. Wang, N. Smith, M. Petukh, E. Alexov, DelPhi: a comprehensive suite for DelPhi software and associated resources, *BMC Biophys.* 5 (2012) 1–11.
- [40] Y.C. Zhou, M. Feig, G.W. Wei, Highly accurate biomolecular electrostatics in continuum dielectric environments, *J. Comput. Chem.* 29 (1) (2008) 87–97.
- [41] R.C. Harris, A.H. Boschitsch, M.O. Fenley, Numerical difficulties computing electrostatic potentials near interfaces with the Poisson-Boltzmann equation, *J. Chem. Theory Comput.* 13 (8) (2017) 3945–3951.
- [42] B. Liu, B. Wang, R. Zhao, Y. Tong, G.-W. Wei, ESES: software for Eulerian solvent excluded surface, *J. Comput. Chem.* 38 (2017) 446–466.
- [43] J.A. Ferreira, R.D. Grigorieff, On the supraconvergence of elliptic finite difference schemes, *Appl. Numer. Math.* 28 (2–4) (1998) 275–292.
- [44] Y.-K. Yu, Electrostatics of charged dielectric spheres with application to biological systems. III. Rigorous ionic screening at the Debye-Hückel level, *Phys. Rev. E* 102 (2020) 052404.
- [45] O.I. Obolensky, T.P. Doerr, Y.-K. Yu, Rigorous treatment of pairwise and many-body electrostatic interactions among dielectric spheres at the Debye-Hückel level, *Eur. Phys. J. E* 44 (2021) 129.
- [46] Y.-K. Yu, Electrostatics of charged dielectric spheres with application to biological systems. II. A formalism bypassing Wigner rotation matrices, *Phys. Rev. E* 100 (2019) 012401.
- [47] R.C. Harris, A.H. Boschitsch, M.O. Fenley, Influence of grid spacing in Poisson-Boltzmann equation binding energy estimation, *J. Chem. Theory Comput.* 9 (8) (2013) 3677–3685.
- [48] A.H. Boschitsch, M.O. Fenley, A fast and robust Poisson-Boltzmann solver based on adaptive Cartesian grids, *J. Chem. Theory Comput.* 7 (5) (2011) 1524–1540.
- [49] J. Wang, C. Tan, Y.-H. Tan, Q. Lu, R. Luo, Poisson-Boltzmann solvents in molecular dynamics simulations, *Commun. Comput. Phys.* 3 (5) (2008) 1010–1031.
- [50] N.A. Baker, D. Sept, S. Joseph, M.J. Holst, J.A. McCammon, Electrostatics of nanosystems: application to microtubules and the ribosome, *Proc. Natl. Acad. Sci. USA* 98 (18) (2001) 10037–10041.
- [51] M. Bosy, M.W. Scroggs, T. Betcke, E. Burman, C.D. Cooper, Coupling finite and boundary element methods to solve the Poisson-Boltzmann equation for electrostatics in molecular solvation, *J. Comput. Chem.* 45 (11) (2024) 787–797.
- [52] D.D. Nguyen, B. Wang, G.-W. Wei, Accurate, robust, and reliable calculations of Poisson-Boltzmann binding energies, *J. Comput. Chem.* 38 (13) (2017) 941–948.
- [53] M. Politi, A scalable solver for the linearized Poisson-Boltzmann equation on Cartesian grids with hierarchical local refinement, Master's thesis, Politecnico di Milano, 2020–2021.
- [54] M. Guerrero-Montero, M. Bosy, C.D. Cooper, Some challenges of diffused interfaces in implicit-solvent models, *J. Comput. Chem.* 46 (3) (2025) e70036.